Engineering Structures 245 (2021) 112853

Contents lists available at ScienceDirect

Engineering Structures

journal homepage: www.elsevier.com/locate/engstruct

Buckling behavior analysis of prestressed CFRP-reinforced steel columns via FEM and ANN

Lili Hu [a,b], Peng Feng [b,*], Yanran Meng [a], Jian Yang [a]

[a] State Key Laboratory of Ocean Engineering, School of Naval Architecture, Ocean and Civil Engineering, Shanghai Jiao Tong University, Shanghai 200240, China
[b] Key Laboratory of Civil Engineering Safety and Durability of China Education Ministry, Department of Civil Engineering, Tsinghua University, Beijing 100084, China

ARTICLE INFO

Keywords:
Steel column
Prestressed CFRP
Buckling
Finite element method
Parametric study
Artificial neural network

ABSTRACT

Prestressed (PS) carbon fiber reinforced polymer (CFRP)-reinforced steel columns are novel multiparameter systems exhibiting complex nonlinear buckling behavior. In this study, this behavior was investigated with the finite element method (FEM) and an artificial neural network (ANN). First, FEM models of the columns under axial and eccentric compression were built. The numerical and experimental force–displacement curves, failure modes, and CFRP stress–displacement curves were in good agreement. Moreover, the influencing rules of 9 key parameters (i.e., CFRP initial prestressing force, supporting length, eccentricity, steel yield strength, slenderness, CFRP elastic modulus, initial imperfection and boundary conditions) on the buckling capacity and reinforcing efficiency of the reinforced columns were determined. Afterward, 312 datasets from the validated finite element model covering 8 input parameters were generated via the ANSYS parametric design language (APDL). Finally, as ANNs can manage highly complex and computationally intensive nonlinear problems, a practical ANN tool was developed to predict the buckling capacity of PS CFRP-reinforced steel columns.

1. Introduction

The buckling of steel structures under compression is a typical failure mode that occurs suddenly and results in severe damage [1]. Recently, 71 people were trapped and 29 people died after a hotel used as a coronavirus quarantine facility in Quanzhou of Fujian Province, China, collapsed due to the buckling of steel columns [2]. To avoid the tragedies caused by buckling of steel columns, researchers have proposed reinforcing/strengthening methods for steel columns, including the use of externally welded steel plates [3,4] and externally wrapped concrete [5], to increase the cross-section or reduce the effective length of the steel columns. The existing methods have been shown to be efficient in increasing the buckling capacity of steel columns; however, welding introduces initial defects and residual stresses, and the use of concrete increases construction difficulty and time. Consequently, several researchers have considered the use of fiber reinforced polymer (FRP) to enhance the buckling performance of steel columns [6–8] and other behaviors of steel structures [9], which exhibits several advantages such as light weight, good fatigue and corrosion resistance, and convenient construction.

1.1. Concept of PS CFRP-reinforced steel columns

Recently, a prestressed (PS) carbon fiber reinforced polymer (CFRP)-reinforced steel column was proposed in reference [10], as shown in Fig. 1(a), which significantly improved the buckling capacity of the steel column and had a convenient construction process. This structure is composed of PS CFRPs, a steel column, prestressing chairs and anchorages. The implementation method is as follows: First, the CFRPs are placed along the length of the steel column, with the two ends fixed by anchorages. Next, the CFRPs are prestressed by the prestressing chairs. A prestressing chair is composed of a movable plate, a fixed plate, a support plate and two bolts. The bolt has a circular tray at the end, which is inserted into the fixed plate and supported by the support plate. The connection of the fixed plate and bolt is a smooth hole; thus, the bolt can freely rotate within the fixed plate. The movable plate is connected through the bolts with threaded holes. Thus, when the two bolts are simultaneously rotated, the movable steel plate moves away from the fixed steel plate because the vertical displacement of the circular tray is restrained by the support plate, and the CFRP is stretched at the midspan of the steel column. The distance between the movable and support plates is the distance of the CFRP from the web of the steel column,

* Corresponding author.
E-mail address: fengpeng@tsinghua.edu.cn (P. Feng).

https://doi.org/10.1016/j.engstruct.2021.112853
Received 9 March 2021; Received in revised form 4 July 2021; Accepted 11 July 2021
Available online 24 July 2021

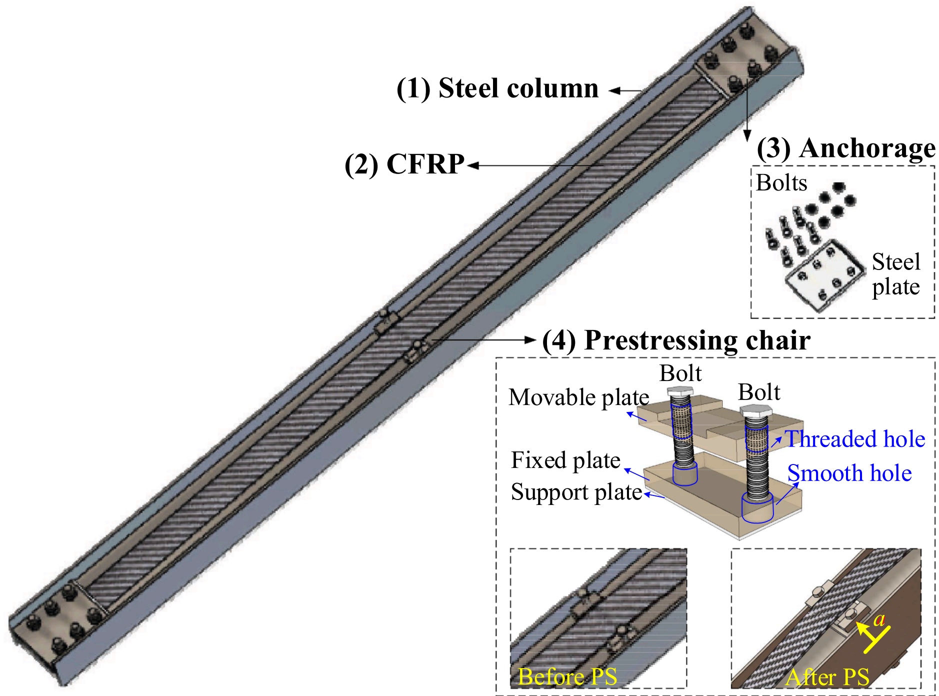

(a) Schematic diagram

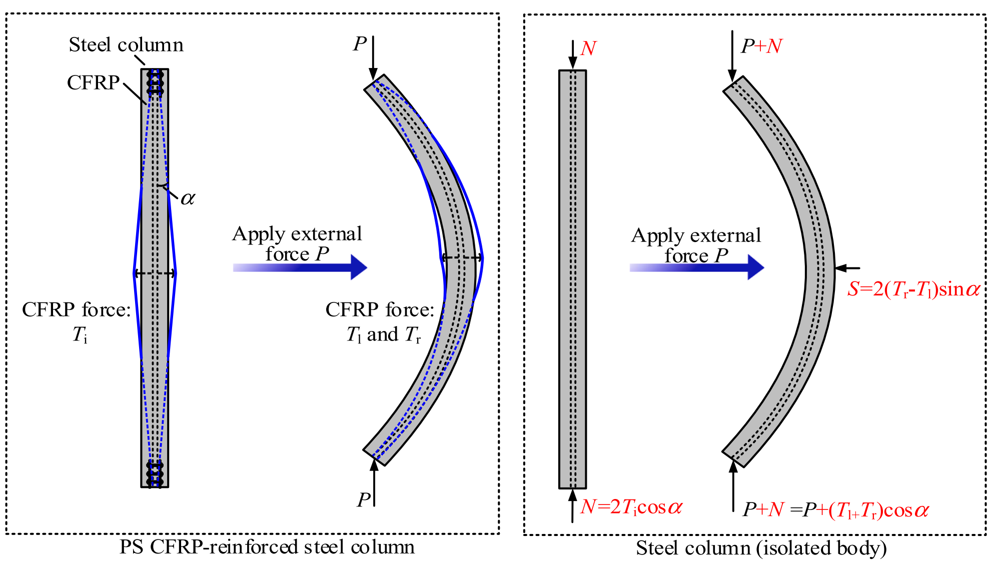

(b) Mechanical system

Fig. 1. PS CFRP-reinforced steel column.

defined as the final supporting length *a*.

Test results have shown that PS CFRP-reinforced steel columns exhibit a buckling capacity that is 2.5 times that of pure steel columns [10,11]. This effective improvement can be attributed to the employed mechanical system, as shown in Fig. 1(b). Assuming the prestressing force of the CFRP is T, subscripts i, l and r represent the initial value before loading, the value in left side and right side, respectively, the angle between the steel column and CFRP is α, and the external compressive force is P, the two forces transferred from the PS CFRP to the steel column (i.e., transverse force S and vertical force N) can be calculated (see Fig. 1(b)). A suitable combination of S and N can generate a high-stiffness system and effectively delay the lateral displacement of the steel column, which is the main reason for the superior buckling performance of this column.

1.2. Knowledge gap and investigation methods

PS CFRP-reinforced steel columns form a complicated system and exhibit a complex and nonlinear buckling behavior. First, the steel has material nonlinearity; second, the geometry is complex because the configuration of the cross section containing CFRPs and steel changes along the column length; third, the CFRPs are prestressed and the slacking of CFRP will change the boundary conditions of the steel column, which is state nonlinearity. In addition, the buckling behavior of the system can be influenced by many parameters, as shown in Fig. 2. The 14 key parameters are listed here. (1) The parameters of the steel column include the length L, elastic modulus E_s, section area A_s, moment of inertia of section I_s, yield strength f_y, and initial imperfection at the midspan v_{om}. (2) The parameters of the CFRP include the elastic

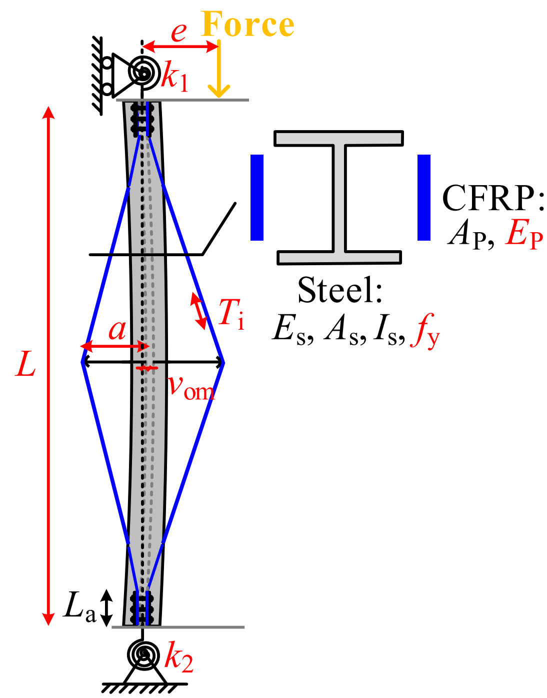

Fig. 2. Fourteen key parameters of the PS CFRP-reinforced steel column (the FEM simulations consider the nine parameters presented in red font). (For interpretation of the references to colour in this figure legend, the reader is referred to the web version of this article.)

modulus E_P and section area A_P. (3) The design parameters include the final supporting length (simply referred to as the supporting length) a, CFRP initial prestressing force T_i, and anchorage length L_a. (4) The parameters of the boundary conditions include the spring stiffnesses of the end supports, k_1 and k_2, both of which range from 0 (hinged support) to $+\infty$ (fixed support), and the load eccentricity e. Owing to these reasons, prediction of the buckling capacity of PS CFRP-reinforced steel columns is complicated.

The conduction of experiments plays an important role in investigating FRP-strengthened steel structures. Owing to the limited experimental results pertaining to PS CFRP-reinforced steel columns, the complex nonlinear buckling behavior of such a complicated system with a wide range of parameters has not been extensively investigated; notably, the influence of the key parameters on the buckling capacity and reinforcing efficiency, and the prediction of the buckling capacity remain unclear. Therefore, the finite element method (FEM) and other tools such as artificial neural networks (ANNs) can be adopted to provide supplementary information to intensively understand the system before a theoretical calculation method and a design method are established.

In this regard, the FEM has been widely utilized to investigate the nonlinear buckling behavior of steel columns [12,13] and FRP-strengthened metal columns [14–17]. For example, Shaat and Fam [14] conducted a nonlinear finite element analysis (FEA) of axially loaded slender hollow structural section columns strengthened with high-modulus CFRP. This model, which was verified against experimental results and results obtained via other analytical models, could successfully predict the ultimate loads and failure modes of the considered columns. Devi and Amanat [15] presented a numerical finite element investigation regarding the behavior of steel square hollow structural section columns strengthened with CFRP; the results of the numerical analysis and past experimental results exhibited good agreement. Feng et al. [16] performed a compression buckling analysis via FEA to study the unique partial elastic buckling behavior of long CFRP-aluminum alloy hybrid columns and observed good agreement between the FEA and buckling test results. In addition, PS CFRP-reinforced steel columns involve a mechanical system that is similar to that of prestressed steel stayed columns [18], and the buckling behavior of the latter type of columns has been analyzed via the FEM [19–21]. It can be seen that the numerical model demonstrated the ability to simulate the nonlinear buckling behavior of slender steel columns and composite columns with a high degree of accuracy.

Furthermore, following the development of machine learning approaches, ANNs have exhibited excellent performance in processing classification and regression tasks and have been successfully applied in risk prediction [22], design optimization [23], health monitoring [24] and damage detection [25] applications. Therefore, this study developed extensive finite element models and applied the ANN method to investigate the buckling behavior of PS CFRP-reinforced steel columns to thoroughly fill the knowledge gap.

1.3. *Structure of the study*

The current study aims to present an in-depth analysis of the buckling behavior of PS CFRP-reinforced steel columns. Following Section 2, which summarizes the existing experimental work, this paper is divided into two main parts. The first part includes Sections 3 and 4, which present the numerical investigations of the influence of 9 main key parameters (parameters presented in red font in Fig. 2) on the buckling behavior of PS CFRP-reinforced steel columns and reinforcing efficiency of PS CFRP, performed after the performance of the FEM was verified against the test results reported previously [10,11]. The second part pertains to Section 5. Based on the datasets generated using the reliable finite element model, ANN-based methods, which can effectively manage complex and highly nonlinear problems, are applied to develop a flexible model to predict the buckling capacity of PS CFRP-reinforced steel columns. A practical approach is derived based on the proposed ANN model, which provides prompt predictions and helps achieve a high reinforcing efficiency.

2. Summary of the experimental work

In references [10,11], compression tests were performed on 12 I-section steel columns with 3 different forms (U, S and PS, as shown in Fig. 3), 3 slenderness values (105, 140, and 200) and 4 different eccentric ratios (0, 1, 2, and 3). U represents unreinforced specimens; S represents steel columns with non-PS CFRPs; PS represents steel columns with PS CFRPs. The section sizes of the steel and CFRP are listed in Table 1, where b is the width of the steel flange; h is the height of the steel section; t_f, t_w, and t_P represent the thickness values of the steel flange, steel web, and CFRP plate, respectively; and b_P is the width of the CFRP plate. The material properties are listed in Table 2. Details of the test specimens are presented in Table 3, where λ is the slenderness of the steel column, and L_e is the effective length of the steel column, which is the sum of L, the thickness of the 2 end plates (i.e., 20 mm) and the double distance from the hinge to the end plate (i.e., 50 mm).

The boundary conditions of all the test specimens were as follows: The compression force was applied by a 500-ton hydraulic pressure testing machine. The specimens with 10-mm-thick end plates at both ends were fixed using a one-way hinge support such that the column could buckle around the weak axis of the I-section steel column. Prior to loading, five percent of the target load was preloaded to the specimen to ensure good contact between the specimen and bearing and later unloaded to remove any misalignment. Next, the columns were loaded at a loading rate ranging from 0.1 to 0.3 kN/s.

3. Numerical modeling and experimental validation

3.1. *Numerical modeling*

Compression buckling analysis was performed using ANSYS [26].

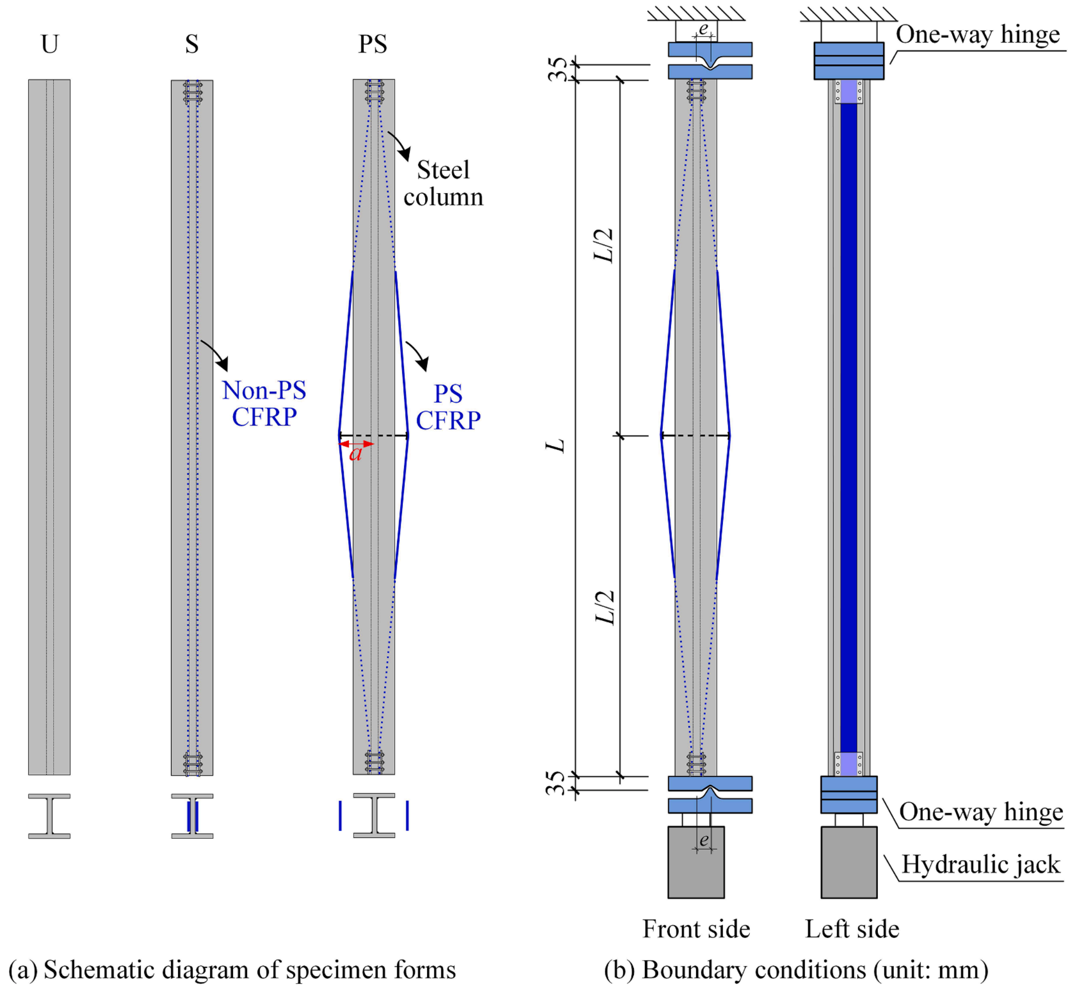

Fig. 3. Schematic diagram of specimens in U, S and PS forms and boundary conditions [10,11].

Table 1
Section dimensions of the steel and CFRP [10,11].

b	h	t_f	t_w	t_P	b_P
70 mm	114 mm	5 mm	5 mm	3 mm	50 mm

Table 2
Material properties of the steel and CFRP [10,11].

Material	Yield strength (MPa)	Ultimate strength (MPa)	Elastic modulus (GPa)
Q690 steel	682	765	$E_s = 206$
Q420 steel	401	564	$E_s = 206$
CFRP	–	2450	$E_P = 171$

APDL was applied to realize parametric modeling and analysis to achieve optimization. On the basis of the nonlinear global instability modeling of pure steel columns [12,13], FRP-strengthened metal columns [14–17] and prestressed steel stayed columns [19–21], numerical modeling for steel columns with PS CFRPs was conducted through the following steps. Numerical modeling for pure steel columns and steel columns with non-PS CFRPs were conducted using a similar method, which were not presented.

3.1.1. Geometric modeling with elements

The geometric model of the steel columns with PS CFRPs is shown in Fig. 4. The steel column was meshed using three-dimensional structural solid elements. Since the steel columns have small width-to-thickness ratios, local buckling was not considered. The commonly used three-dimensional solid elements, including 8-node SOLID45 elements and 20-node SOLID95 elements, were implemented. Because the difference in the calculation results of the two solid elements in this model was extremely small, the 8-node SOLID45 elements, which have fewer nodes, were used to reduce the calculation time and increase the calculation efficiency.

The CFRP was meshed using LINK10 element, which is three-dimensional spar element that can simulate the tension-only behavior of a slack CFRP. The cross-section of the LINK10 elements was set according to the real section of the CFRP. When modeling the CFRP, the geometric model was simplified as follows. In a real specimen, the CFRP goes through the full length of the steel column, has a certain bending arc in the middle of the span, and can slide relative to the prestressing chair at the midspan. Since most of the specimens exhibited symmetrical buckling modes and the upper and lower CFRPs sustained the same deformation, no relative slippage occurred between the CFRP and prestressing chair; this behavior was verified through tests. In addition, for specimens that exhibited asymmetric buckling (i.e., I140-PS), the relative slippage between the CFRP and prestressing chair was very small, as observed in the tests. This phenomenon could be attributed to the following aspect: because the CFRP was prestressed, a high pressure was generated between the CFRP and movable plate of the prestressing

Table 3
Test specimens [10,11].

Specimen		λ	Reinforcing method	L (mm)	L_e (mm)	L_a (mm)	T_i/A_P (MPa)	a (mm)	e (mm)	Steel
Axial loading group	I105-S	105	Non-PS CFRP	1620	1690	130	0	0	0	Q690
	I105-PS	105	PS CFRP	1619	1689	130	123	41	0	Q690
	I140-U	140	–	2148	2218	130	–	–	0	Q690
	I140-S	140	Non-PS CFRP	2150	2220	130	0	0	0	Q690
	I140-PS	140	PS CFRP	2154	2224	130	302	70	0	Q690
	I200-S	200	Non-PS CFRP	3070	3140	200	0	0	0	Q690
	I200-PS	200	PS CFRP	3065	3135	200	146	78	0	Q690
Eccentric loading group	I105-PS-e0	105	PS CFRP	1621	1691	130	190	53	0	Q420
	I105-PS-e1	105	PS CFRP	1615	1685	130	220	55	14	Q420
	I105-PS-e2	105	PS CFRP	1616	1686	130	160	53	31	Q420
	I105-PS-e3	105	PS CFRP	1619	1689	130	150	51	43	Q420

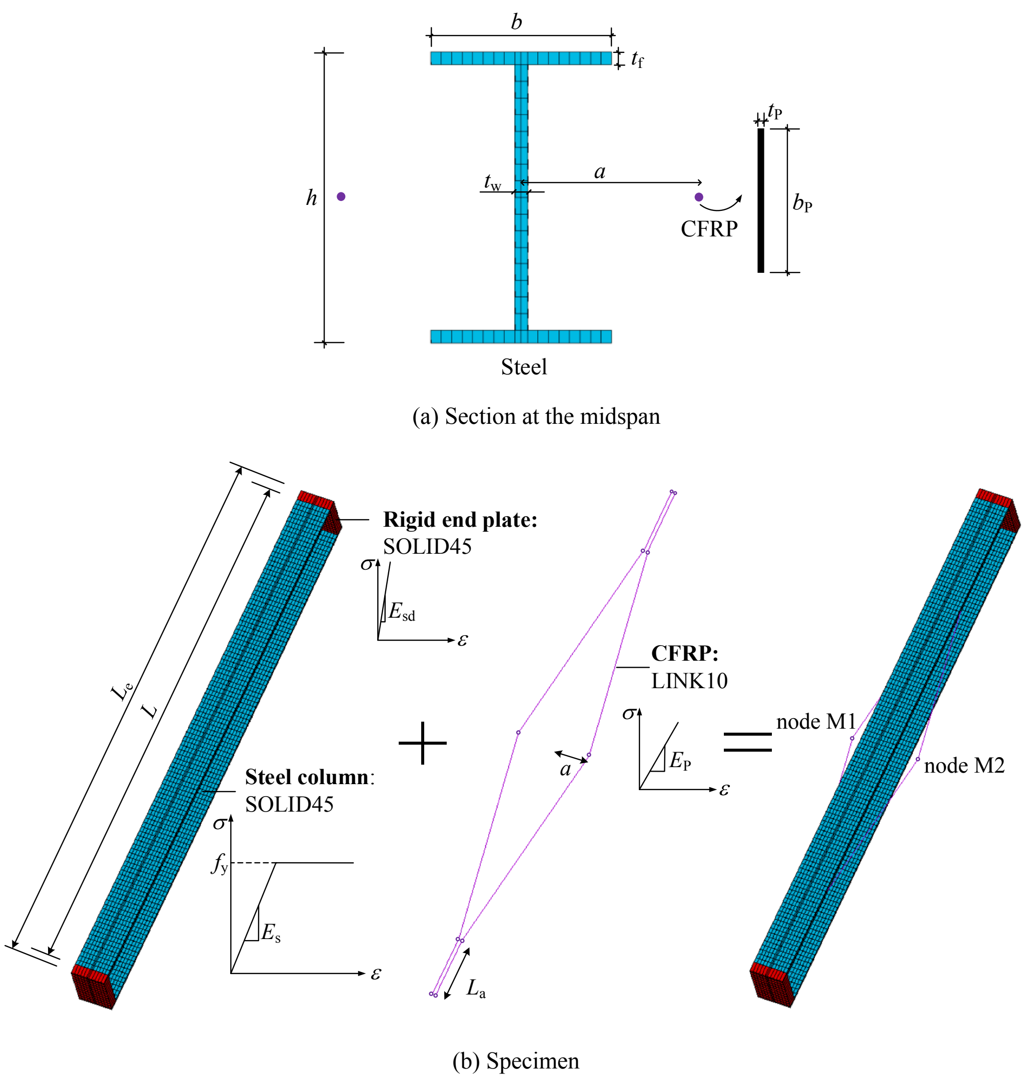

Fig. 4. Geometric finite element model with element types and materials.

chair, which increased the frictional force between the two entities; thus, slippage did not occur easily. Therefore, this paper simplified the CFRP on each side by connecting two linear elements with hinged joints at nodes M1 and M2, as shown in Fig. 4(b).

The anchorage was modeled as follows. Owing to the effective function of the anchorage, no debonding or rupture occurred in the tests [10,11], which meant that the two ends of the CFRP did not separate from the steel column. Hence, all the degrees of freedom of the nodes of the CFRP and corresponding nodes of the steel column at the anchorage zones were coupled, as shown in Fig. 4.

The prestressing chair was modeled as follows. The convex-side CFRP was never separated from the prestressing chair; although the concave-side CFRP separated from the prestressing chair after becoming slack, the slack CFRP did not affect the buckling capacity or deformation of the steel column. In addition, the compression of the prestressing chair was negligible. Thus, all the degrees of freedom of the nodes at the

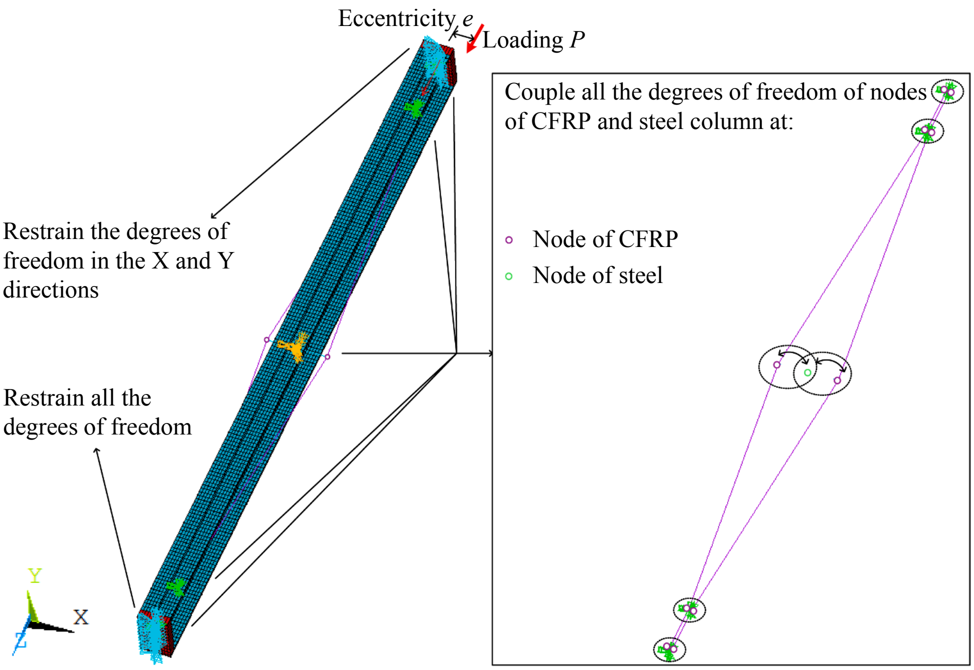

Fig. 5. Modeling of anchorage and prestressing chair including the boundary conditions.

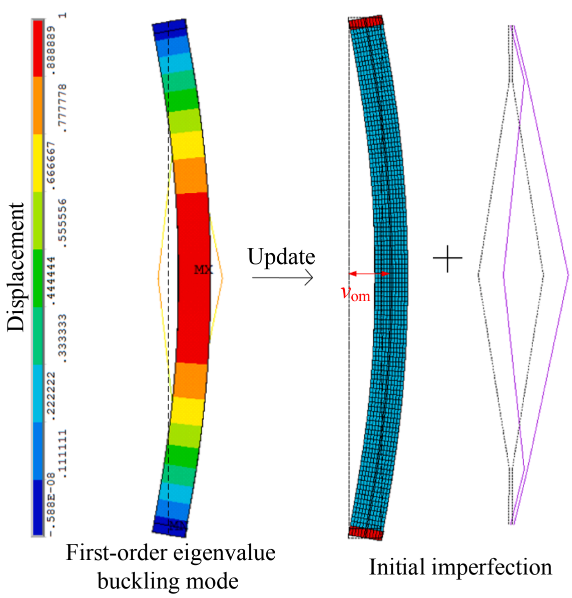

Fig. 6. Adding geometric imperfection.

center of the midspan of the steel column web and nodes M1 and M2 were coupled to realize the function of the prestressing chair, as shown in Fig. 5.

To model the steel column, the SOLID45 elements were divided into an average length of 10 mm along the axis of the steel column; the maximum lengths along the steel flange and web directions were 8.125 mm and 10.4 mm, respectively. The LINK10 elements did not need to be divided [27]. After the convergence check, the refinement of the elements was found to be sufficient.

3.1.2. Material and prestressing of the CFRP

Considering the plastic development of steel, the material constitutive model for steel columns can be either a multilinear model considering the hardening or a simplified ideal elastoplastic model. In the case of steels with obvious yielding plateaus, the compression members usually do not enter strain hardening when overall buckling occurs [28]. Hence, a simplified ideal elastoplastic model and bilinear isotropic hardening material model were used as the constitutive models for steel.

CFRP has high strength (i.e., 2450 MPa) and does not commonly fail during tests when used as reinforcement for steel components. Thus, a linear elastic constitutive material model was adopted for the CFRP, and the elastic modulus of the CFRP was set as the value of E_P in Table 2. The prestress of CFRP can be set by changing its real constant [27,29]. Since the axial compression stiffness of the steel column is not infinite, the steel column reinforced with CFRP is expected to self-balance after the application of the CFRP prestress, after which, the CFRP prestress is reduced. In this paper, the CFRP prestress before self-balancing, which was input to the FEM simulation, was defined as T_{input}. Since the CFRP prestress after self-balancing corresponded to the real prestress of the CFRP before the test loading, it was defined as T_{real}. The value of T_{real} was dependent on T_{input} and the axial stiffness values of the CFRP and steel column, which could be obtained in the first loading step.

The end plates of the steel column, as in the case of the steel column, were modeled with 8-node SOLID45 elements. To ensure that the end plate did not deform under loading, its elastic modulus E_{sd} was set as 1000 times the steel elastic modulus E_s to form a rigid end plate.

CO_2 gas shielded arc welding was performed to control the welding deformation [30], and the flatness of the steel column was adjusted after welding to satisfy the requirements of component flatness; thus, most of the residual stress was released, and the effect of the residual stress was not considered.

3.1.3. Boundary conditions and loading

Rigid end plates were placed at both ends of the specimen to restrain the specimen and transfer loads via the SOLID45 elements. All the degrees of freedom were coupled at the shared nodes between the rigid plate and specimen.

For all the nodes on the weak axis of the bottom end, the translations in all the directions (i.e., UX, UY and UZ) were constrained. For all the nodes on the weak axis of the upper end, the translations in the X and Y directions (i.e., UX and UY) were constrained to represent the hinged supports. The external load P was applied at the central point or at an eccentricity e from the central point at the end plate in the Z direction.

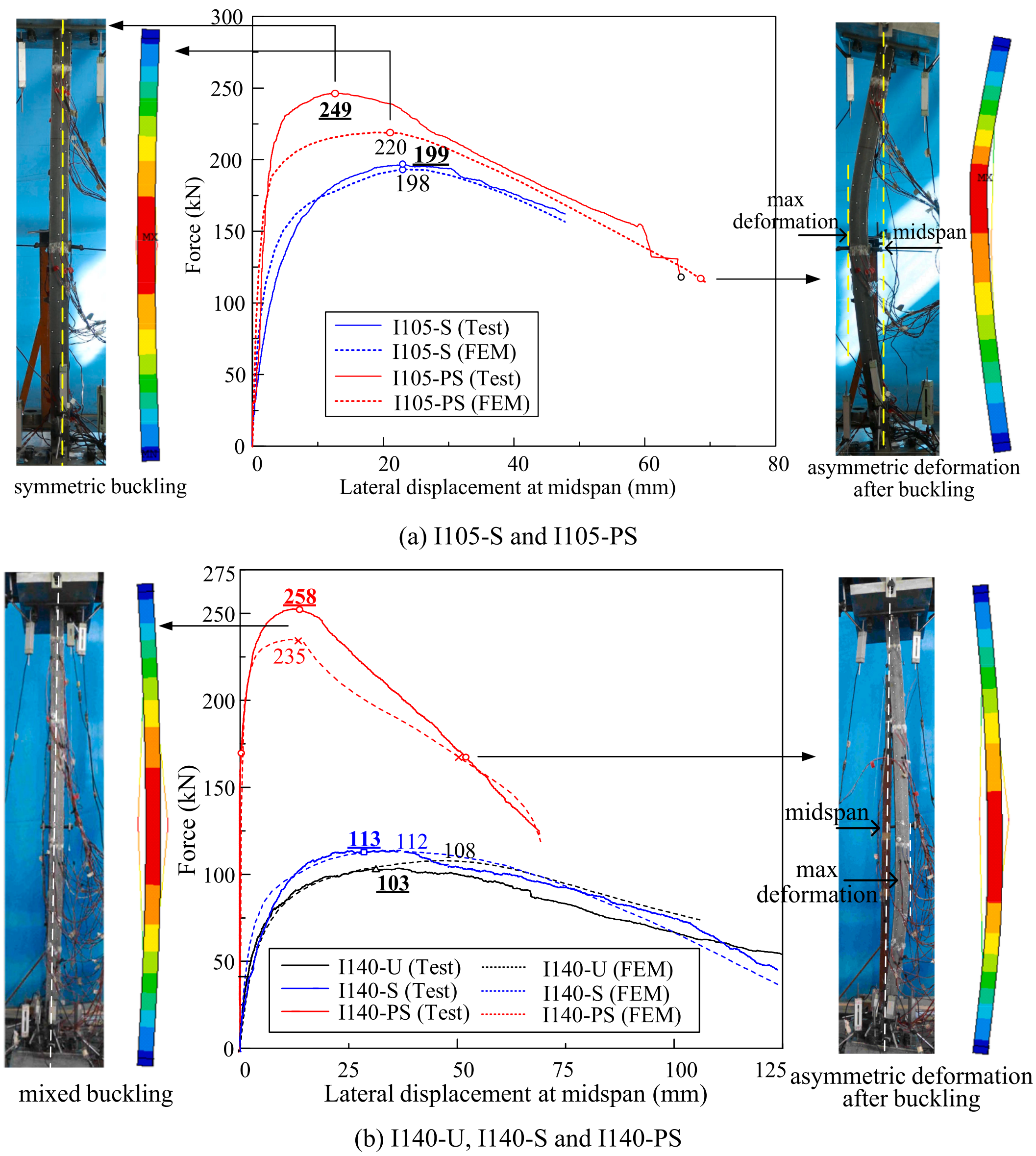

Fig. 7. Comparison of force–displacement curves and failure modes obtained from the FEM simulations and tests.

3.1.4. Calculation

An eigenvalue buckling analysis was conducted to obtain the eigenvalue buckling load and first-order buckling mode. The geometric stiffness of the component changed after the prestress was applied; consequently, when solving the eigenvalue buckling load, the prestress was maintained at a constant value, and the external load iteration was changed continuously until the eigenvalue became 1.0. The corresponding external load was the eigenvalue buckling load [31].

Reference [32] indicated that the initial geometric imperfection distribution of most specimens was close to a single-wave sinusoid, and the initial geometric imperfection at the midspan was between 0.02%L and 0.15%L, as determined by three-dimensional laser scanning. Therefore, the first-order mode of the eigenvalue buckling was multiplied with the measured initial defect value (for the measured component) or 0.15%L (for the unmeasured component), and the product was added to the original model as the initial geometric imperfection, as shown in Fig. 6.

Finally, considering the influence of the large deformation, nonlinear buckling analysis was conducted using the arc length method. This approach can automatically adjust several factors, including the arc length radius range and maximum balance iteration number, and determine the extreme point buckling capacity. In addition, the implemented approach can obtain the descending segment of the load–displacement curve more easily than other iteration methods.

3.2. Experimental validation

Before using the numerical model, it was necessary to validate the model with the experimental results reported in references [10,11]. The geometric model, material properties and CFRP prestress were based on the real test, as shown in Tables 1–3, respectively. Specifically, because the difference between L_e and L was 70 mm, the thickness of one rigid end plate was 35 mm. Comparisons of the force–lateral displacement curves and failure modes (i.e., symmetric buckling or mixed buckling) are shown in Fig. 7. For the force–lateral displacement curves, the stiffness results of all the specimens, as obtained from the FEM simulation and test were in good agreement. The boldfaced and underlined numbers in Fig. 7 represent the buckling capacities measured in the tests, whereas the numbers in the standard font indicate the buckling capacities calculated through the FEM. The buckling capacities of all the

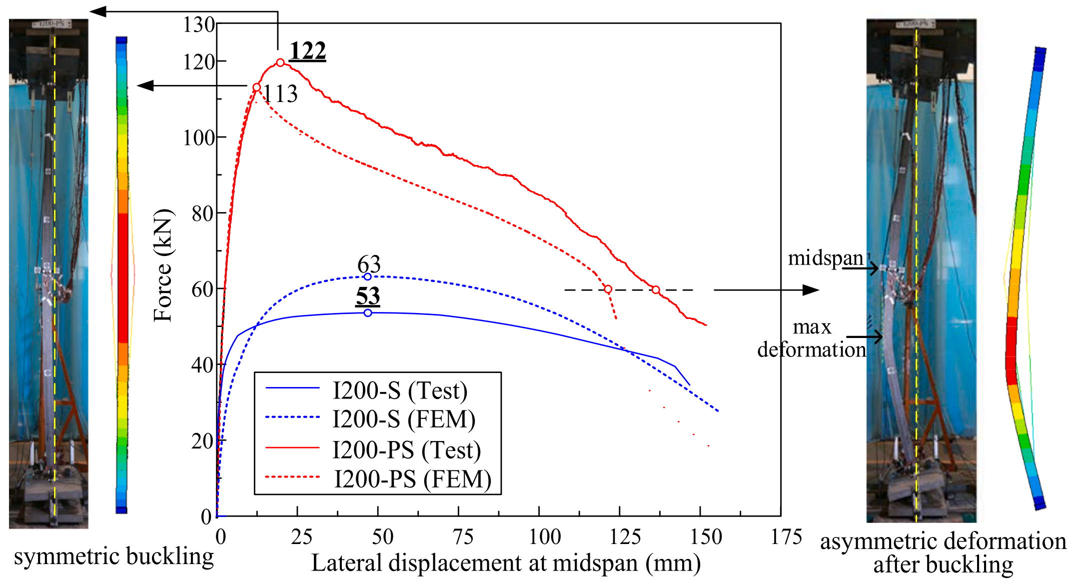

(c) I200-S and I200-PS

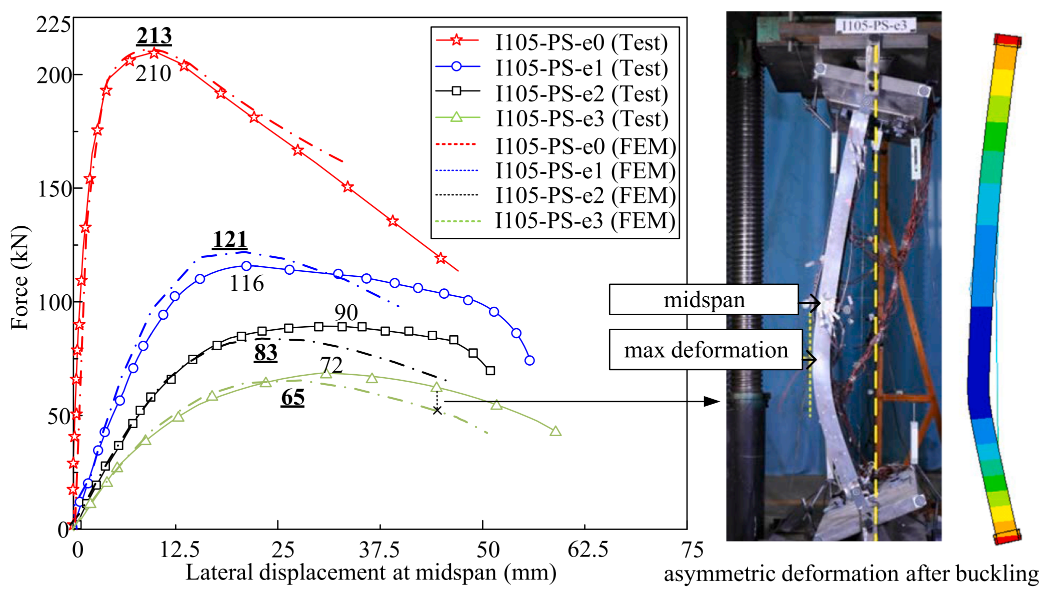

(d) I105-PS-e0, I105-PS-e1, I105-PS-e2, and I105-PS-e3

Fig. 7. (*continued*).

reinforced specimens and specimen I140-U (12 specimens), as determined through the tests and FEM simulations, are compared in Fig. 8, where I105 series include all the specimens with λ of 105 in Table 3. The ratio of the buckling capacity obtained from the FEM to that obtained in the test was between 0.88 and 1.05, with an average value of 0.97. The difference in the FEM and test results can be attributed to the following aspect: the initial defect distribution of the real component was not an exact standard single-wave sinusoid [32], and the FEM did not consider the effect of the residual stress.

Furthermore, the FEM successfully simulated the failure modes and deformation after buckling of the test specimens. Specifically, the pure steel columns and steel columns reinforced by non-PS CFRP exhibited symmetrical buckling modes, and the deformation remained symmetrical after buckling occurred. Most of the steel columns reinforced by PS CFRP exhibited symmetrical buckling and later sustained asymmetrical deformation after buckling; only I140-PS exhibited a mixed buckling mode. Although the geometric model and initial imperfection considered in this paper were symmetrical, it could simulate asymmetrical deformation, in which the maximum lateral displacement appeared at random in the upper or lower part of the steel column. The location of the maximum lateral displacement from the FEM simulations was consistent with the test results.

Furthermore, in terms of the changes in the CFRP stress with respect to the lateral displacement at the steel column midspan, the FEM results were in good agreement with the test results, as shown in Fig. 9. Basically, the CFRP stress of the PS CFRP-reinforced specimens under axial loading decreased in the first step, and the stress of the concave-side CFRP continued to decrease while that of the convex-side CFRP started to increase; the CFRP stress of the PS CFRP-reinforced specimens under eccentric loading did not exhibit the trend of the first step. These results verified the accuracy of the numerical modeling, and parametric studies were carried out with this model.

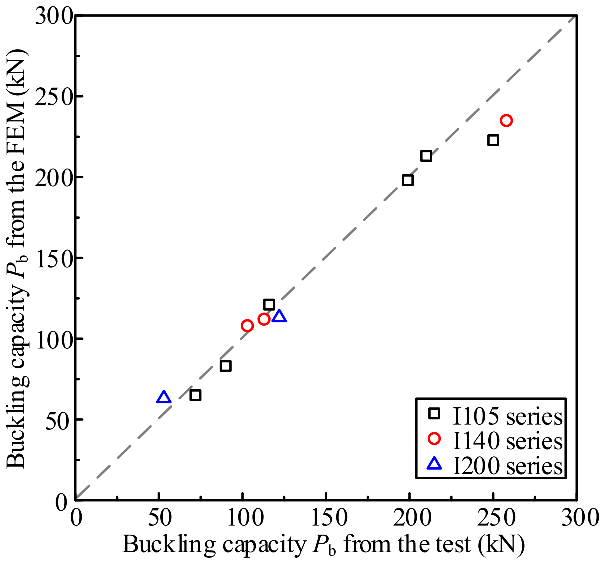

Fig. 8. Comparison of buckling capacities obtained from the FEM simulations and tests.

4. Parametric study

Parametric studies were performed considering 9 key parameters that effect the behavior of the steel columns reinforced with PS CFRPs, as shown by in red font in Fig. 2. Because the elastic modulus of steel lay in a small range (i.e., 201–206 GPa), it was not included in the parametric studies. In the following analysis, the buckling capacity of the reinforced specimen and unreinforced steel column were defined as $P_{b,s}$ and $P_{b,u}$, respectively, and the reinforcing efficiency was defined as $P_{b,s}/P_{b,u}$. The optimal CFRP initial prestressing force, which attained the maximum buckling capacity ($P_{b,max}$), was defined as T_{opt}, and the corresponding optimal reinforcing efficiency was defined as $P_{b,max}/P_{b,u}$.

4.1. Influence of the CFRP initial prestressing force T_i and supporting length a

4.1.1. Relationship between T_i and a

When a certain steel column is reinforced by a certain CFRP, the two key design parameters that determine the buckling behavior and reinforcing efficiency of the reinforced steel column are the supporting length a and CFRP initial prestressing force T_i. To obtain the influencing tendency of T_i and a on the reinforcing efficiency $P_{b,s}/P_{b,u}$ and failure mode, it is necessary to first determine the relationship between T_i and a. When the CFRP was stretched with only the prestressing chair and no additional tensioning devices, the CFRP prestressing force increased from 0 to T_i during the construction process with the supporting length increasing from the initial length a_0 to the final length a. Therefore, T_i and a can be independent within a certain range, and the relationship between T_i and a was determined by a_0.

Three relationships exist between T_i and a, as shown in Fig. 10. (1) When a_0 is 0, T_i can achieve its maximum value T_{max}. (2) When $0 < a_0 < a$, $0 < T_i < T_{max}$. (3) When a_0 is a, T_i achieves its minimum value T_{min} (i.e., 0). Thus, T_i has two bounds, T_{max} and T_{min}, and the range between the two bounds can be determined by the value of a_0. When considering the anchorage length L_a, based on the geometric deformation of the CFRP, T_i can be calculated by Eqs. (1)–(3), where $L_{P,0}$ and L_P represent the length of the CFRP before and after prestressing, respectively. Specifically, T_{max} can be obtained by Eq. (4).

$$T_i = (L_P - L_{P,0})/L_{P,0} \cdot E_P A_P \tag{1}$$

$$L_P = 2\sqrt{(L/2 - L_a)^2 + a^2} \tag{2}$$

$$L_{P,0} = 2\sqrt{(L/2 - L_a)^2 + a_0^2} \tag{3}$$

$$T_{max}(a) = \frac{2\sqrt{(L/2 - L_a)^2 + a^2} - (L - 2L_a)}{(L - 2L_a)} \cdot E_P A_P \tag{4}$$

4.1.2. Results and analysis under axial loading

In this section, I140-PS is taken as an example. All parameters were the same as those for I140-PS, only T_i and a were changed, and the initial imperfection was a full sine wave with a maximum value of 0.02%L at the midspan. The buckling capacity $P_{b,u}$ of the unreinforced specimen corresponding to I140-PS was 117.2 kN, according to the FEM simulation.

The range of a was set from 0 to 130 mm in intervals of 10 mm. For a certain value of a, the range of T_i was set from 0 to T_{max} in intervals of 6 to 15 kN. Thus, 108 specimens were simulated, labeled Cases 1 to 108, respectively. In Fig. 11(a), a, T_i and their corresponding reinforcing efficiencies ($P_{b,s}/P_{b,u}$) are drawn in three-dimensional space, and Fig. 11 (b) shows the corresponding projection on the X-Y plane. The two bounds of T_i are T_{max} and T_{min}. The former and latter bounds represent a parabolic curve and straight line, respectively. The gray area in the middle can be obtained by designing the initial supporting length a_0. Fig. 11(c) shows the projection of the three-dimensional space on the X-Z plane. After the relationship between T_i and a is determined, $P_{b,s}/P_{b,u}$ can be determined. In addition to setting T_i equal to T_{max} and T_{min}, T_i can be kept unchanged by changing a_0 and a. In this case, T_i that remains unchanged with a is $T_{certain}$. Fig. 12 shows the different buckling modes of all the abovementioned cases. The following sections describes a specific analysis of cases in which $T_i = T_{max}$, $T_i = T_{certain}$, and $T_i = T_{min}$.

4.1.2.1. $T_i = T_{max}$. When $T_i = T_{max}$, as the value of a increased from 10 mm to 120 mm, T_i/A_P increased from 10 MPa to 1373 MPa, and the corresponding situations were labeled Cases A-1 to A-12, as shown in Table 4, selected from Cases 1 to 108. The results indicated that as a increased, $P_{b,s}/P_{b,u}$ first increased and later decreased, and the buckling mode changed from symmetric to mixed to antisymmetric.

Fig. 13(a) shows the force–lateral displacement curves. Case A-3 was the optimal situation with the highest buckling capacity and initial stiffness. The results of Cases A-11 and A-12 were nearly similar to those of the unreinforced specimen; hence, the reinforcing efficiency in these cases was quite limited.

Fig. 13(c) shows the stress of the concave- and convex-side CFRPs and the lateral displacement at the midspan. In this configuration, the stress of the CFRPs on both sides first decreased; later, the stresses of the convex-side and concave-side CFRPs increased and decreased, respectively, thereby generating a horizontal force S. On the basis of T_{real} and Fig. 1, the values of S_l (equal to S_r), S, and N after prestressing were calculated, and the corresponding values at the onset of buckling were extracted from the finite element results, as shown in Table 4 and Fig. 13 (b) and (d). As shown in Fig. 13(b), S_l/N after prestressing increased linearly with increasing a. When $S_l/N \geqslant 1.1\%$, $P_{b,s}/P_{b,u} \geqslant 1.01$, meaning that the reinforcing system took effect. When $S_l/N = 5.3\%$, $P_{b,s}/P_{b,u} = 2.52$, and the optimal situation occurred. When $S_l/N \geqslant 5.3\%$, $N \geqslant 0.57 P_{b,s}$, and $P_{b,s}/P_{b,u}$ started to decrease because N was too high compared to S. As shown in Fig. 13(d), as a increased, S first increased and later started to decrease when the mixed and antisymmetric buckling modes occurred. This phenomenon occurred because the value of S was related to the deformation of the CFRPs on both sides. The mixed and antisymmetric buckling modes did not lead to a significant difference in the stresses of the concave- and convex-side CFRPs. In addition, N increased with increasing a at an increasingly higher rate.

In summary, when $T_i = T_{input} = T_{max}$, the optimal reinforcing efficiency occurred when the value of a led to a mixed buckling mode; when the value of a led to a symmetrical buckling mode, a higher a corresponded to a higher S at the onset of buckling and higher reinforcing efficiency.

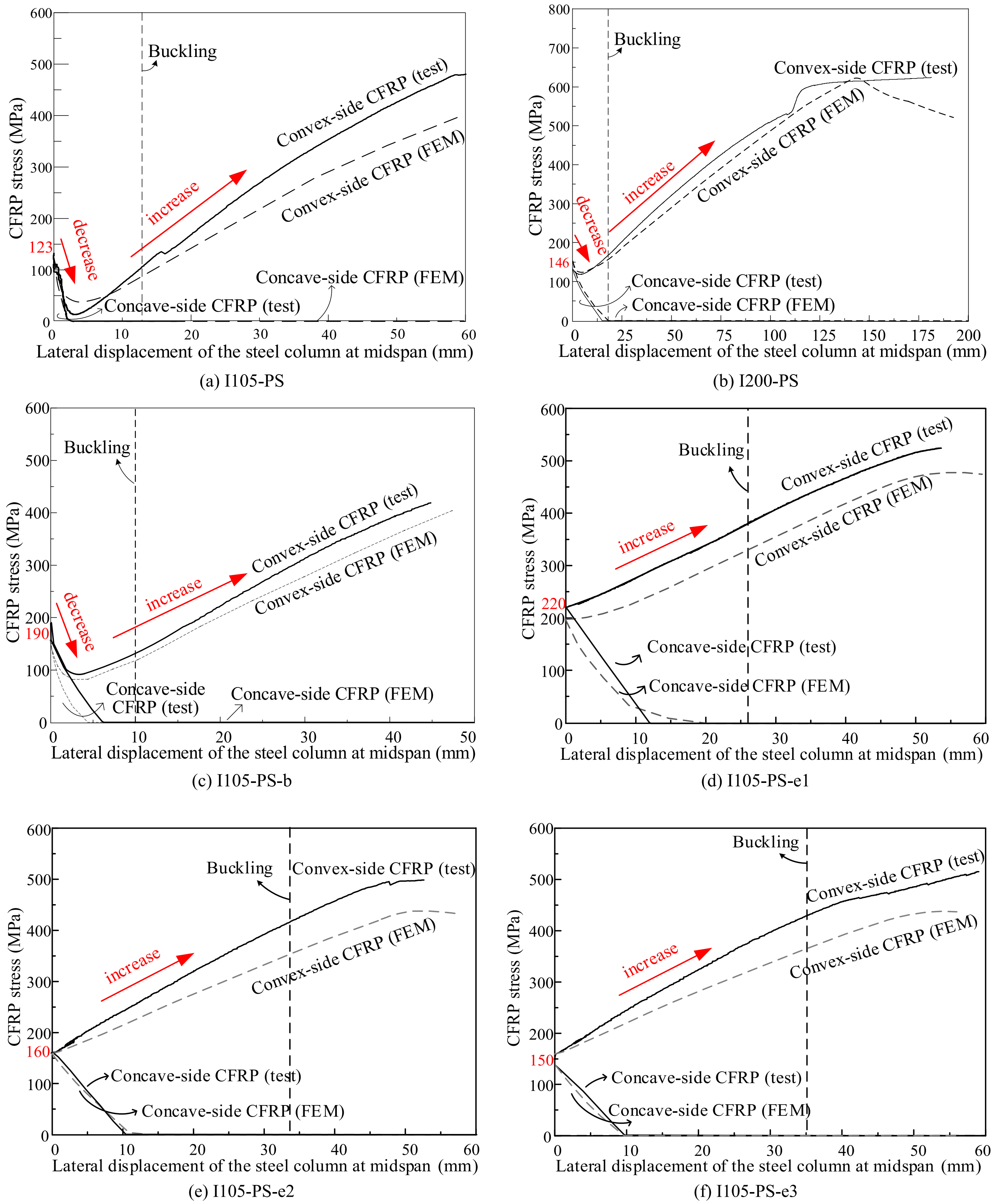

Fig. 9. Comparison of CFRP stress-lateral displacement curves obtained from the FEM simulations and tests.

4.1.2.2. $T_i = T_{certain}$. When a ranged from 50 mm to 130 mm, $T_i = T_{input} = T_{certain}$ could be set as approximately 28.8 kN by setting different values of the initial supporting length a_0, leading to the 8 cases shown in Table 5, with Case B-8 being the same as Case A-8 for reference. The 8 cases were selected from Cases 1 to 108. The difference in $T_{certain}$ for each case emerged from rounding the value of a_0.

For this situation, the influence of a on the force–displacement curves and $P_{b,s}/P_{b,u}$ is shown in Table 5 and Fig. 14. The results indicated that as a increased from 50 mm to 130 mm (increase of 160%), $P_{b,s}$ increased from 176.3 kN to 345.0 kN (increase of 96%), and $P_{b,s}/P_{b,u}$ increased, with its highest value being 2.94 when a was 130 mm. At this instant, the buckling mode changed from symmetric to antisymmetric.

In addition, the CFRP stress, S_l/N after prestressing, and S and N at the onset of buckling were obtained. The results indicated that as a

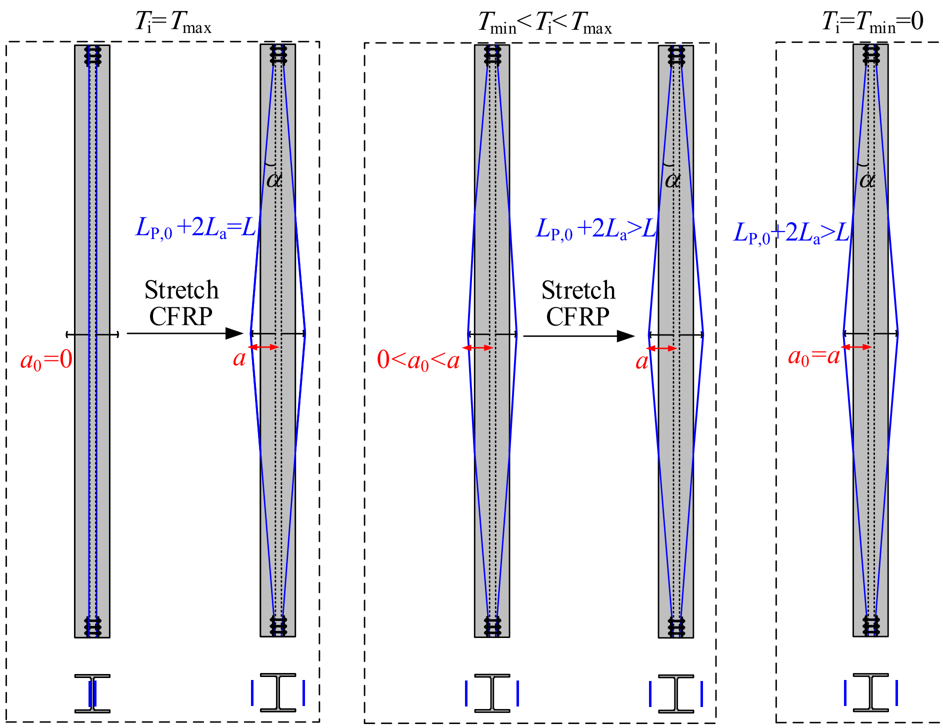

Fig. 10. Three relationships between T_i and a.

increased, S_l/N after prestressing increased; S at the onset of buckling remained very small, which had an obvious decrease when the buckling mode changed from the symmetric mode to antisymmetric mode; N at the onset of buckling decreased because the angle α was the key factor, which increased as a increased.

4.1.2.3. $T_i = T_{min}$. When $T_i = T_{min} = 0$, the values of S_l and N after prestressing were 0. Table 6 shows 13 cases in which a ranges from 10 mm to 130 mm, labeled Cases C-0 to C-12. The 13 cases were selected from Cases 1 to 108. In this situation, the limited reinforcing efficiency was attributed to the small horizontal supporting force S from the convex-side CFRP caused by the lateral displacement of the steel column.

Cases C-0 to C-12 exhibited symmetric buckling modes, and the force–displacement curves were different from those of $T = T_{max}$, as shown in Fig. 15(a). Specifically, the curves were the same at the beginning. When the stiffness started to decrease, an obvious bifurcation occurred, after which the stiffness started to increase and the 13 curves began to differ from one another: a larger a corresponded to a higher stiffness after the bifurcation and higher buckling capacity. This phenomenon occurred because the convex-side CFRP could be adequately stretched to generate a high S to resist lateral deformation only if the lateral displacement at midspan is sufficient large.

Fig. 15(b) and (c) show the change in the CFRP stress with respect to the lateral displacement at the midspan. The concave-side CFRP stress remained zero, whereas the convex-side CFRP stress increased as the lateral displacement at the midspan increased. For the specimens with a higher a, the increase was more rapid, and thus, S at the onset of buckling was greater, as shown in Table 6. Thus, the same conclusion was obtained: for specimens exhibiting a symmetric buckling mode, a higher S was beneficial to achieve a higher value of $P_{b,s}/P_{b,u}$.

4.1.2.4. Summary. First, the supporting length a (or the value of a/L) was a crucial parameter influencing the buckling mode. Specifically, when $T_i = T_{max}$, T_i was sufficiently high and caused the concave-side CFRP to remain in tension when buckling occurred. As a increased, the buckling mode changed from symmetric to mixed to antisymmetric buckling, and the optimal reinforcing efficiency $P_{b,s}/P_{b,u}$ was achieved in the mixed buckling mode, similar to the conclusions presented in reference [33]. When $T_i = T_{min}$, T_i was insufficient, and thus, the concave-side CFRP became slack when buckling occurred, and all the buckling modes were symmetric. At this time, as a increased, $P_{b,s}/P_{b,u}$ continued to increase. In addition, when a was constant, if the concave-side CFRP was in tension when buckling occurred, only symmetric buckling occurred, regardless of how large T_i was. At this time, T_i influenced only the reinforcing efficiency and not the buckling mode.

Second, when a was constant, the situation for the optimal CFRP initial prestressing force T_{opt} was as follows: when a was small ($a \leqslant 70$ mm), $T_{opt} \geqslant T_{max}$; when a was relatively high ($70 < a \leqslant 90$ mm), $0 < T_{opt} < T_{max}$; and when a was very high ($a > 90$ mm), $0 < T_{opt} < T_{max}$. In addition, the values of $P_{b,s}/P_{b,u}$ when $T_i = T_{certain} = 28.8$ kN and $T = T_{max}$ were very similar. However, a large difference in $P_{b,s}/P_{b,u}$ was noted when $T = T_{min}$ and the other two situations, and this difference became greater as a increased.

Third, according to the considered 108 cases, the reinforcing efficiency of the PS CFRP was good when suitable values were selected for T_i and a. The maximum reinforcing efficiency was 3.5, which occurred when $a = 130$ mm and $T_i/A_P = 400$ MPa.

Thus, to achieve the maximum reinforcing efficiency, the following suggestions are recommended. To choose the value of a, first, the maximum value of a that leads to symmetric buckling should be identified. Next, this value must be compared with the maximum allowable value of a and the lower value among the two values should be selected. To choose the value of T_i, to obtain a high buckling capacity, T_{opt} or T_{max} can be selected; for projects in which a substantial increase in the buckling capacity is not needed, T_{min} can be selected, in which case, the stress of the deformed CFRP is small, thus the requirements for the strength of the CFRP and anchorage can be accordingly reduced.

4.1.3. Results and analysis under eccentric loading

I105-PS-e3 in Table 3 was taken as an example to study the influence of T_i and a on the buckling capacity and reinforcing efficiency under eccentric loading. All the parameters were derived from Table 3 except the initial imperfection, which was set as 0.02%L; moreover, a was set as

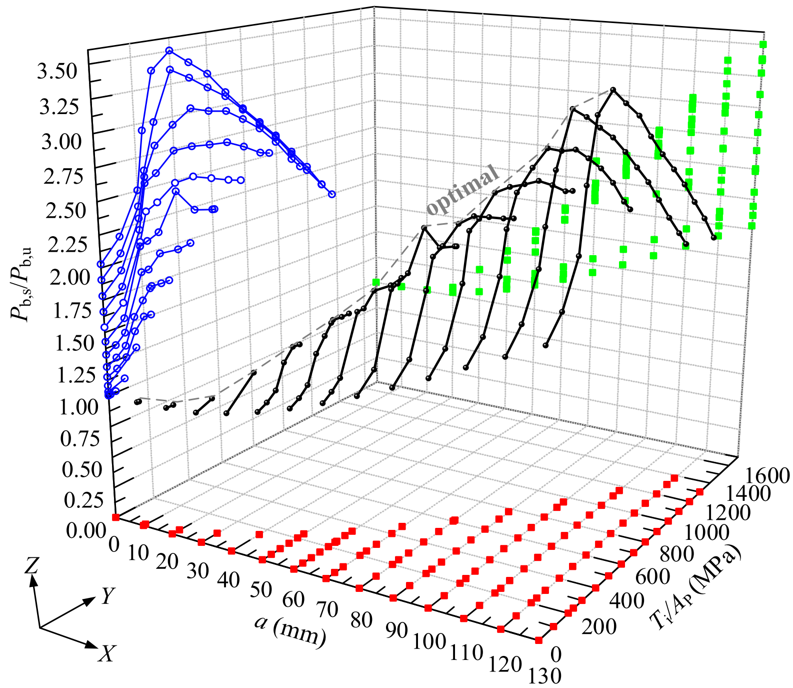

(a) Influence of T_i and a on $P_{b,s}/P_{b,u}$

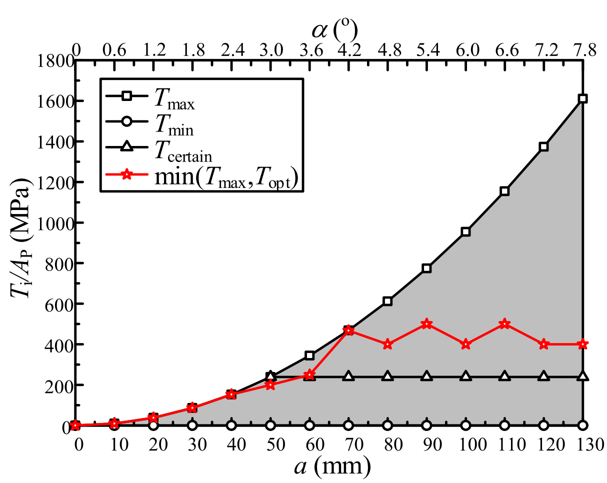

(b) X-Y plane: relationship between T_i and a

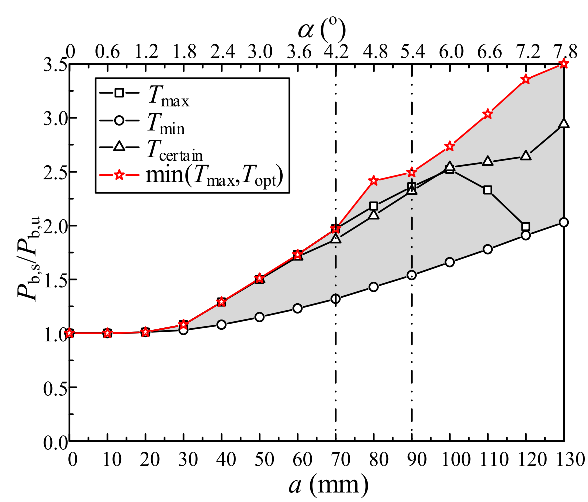

(c) X-Z plane

Fig. 11. Influence of T_i and a on the reinforcing efficiency under axial loading.

a variable from 41 to 80 mm, and the value of $T_i(=T_{input})$ ranged from 0 to T_{max} or T_{opt}. In this manner, 49 cases labeled Cases 109 to 157 were simulated, and the results are shown in a three-dimensional space in Fig. 16. The buckling capacity before reinforcing ($P_{b,u}$) of I105-PS-e3 was 52.8 kN. The influencing tendency of T_i and a on $P_{b,s}$ and $P_{b,s}/P_{b,u}$ under eccentric loading was similar to that under axial loading. It was inferred that this influencing tendency held for specimens with eccentricity ratios no greater than 3.

In the following analyses, the focus was mainly on the influence of the parameters on specimens under axial loading.

4.2. Influence of the steel yield strength and slenderness on specimens under axial loading

In this analysis, the parameters were the same as those listed for I140 in Table 3 except that the initial imperfection was 0.02%L; the slenderness was set as 105, 140 and 200; the steel yield strength f_y was set as 345 MPa, 682 MPa and 960 MPa; and the range of T_i was $T_i = T_{input} \leqslant T_{max}$. Thus, 26 specimens labeled Cases 158 to 183 were designed and simulated. In the specimen labels, I indicates an I-section column, the number following I (i.e., 105/140/200) represents the slenderness, the symbol U following the slenderness represents an unreinforced specimen, the number following the slenderness indicates $\sigma_{PS,P}$ $(=T_i/A_P)$, and the number in the last position represents f_y.

Fig. 17 shows the influence of the slenderness and yield strength on the buckling capacity and reinforcing efficiency. The solid gray symbols in Fig. 17(a) represent the optimal reinforcing situation. The following conclusions could be derived. (1) For specimens with a large slenderness (140 or 200), the influence of the yield strength on the buckling capacity and reinforcing efficiency was very limited because the buckling of long specimens was not controlled by the yield strength. For specimens with a small slenderness (105), when the yield strength increased from 345 to

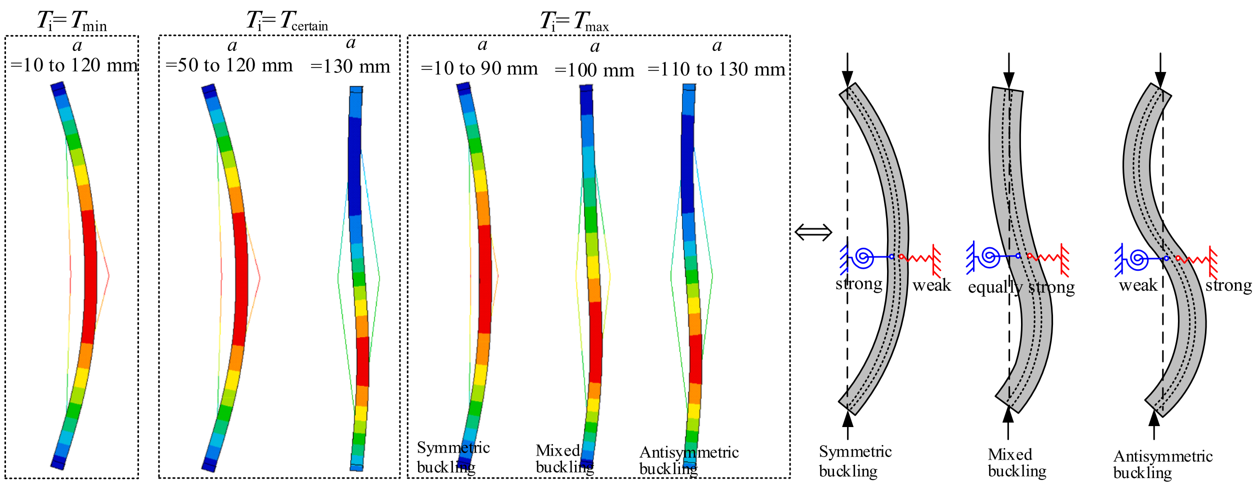

Fig. 12. Buckling modes for all cases in Fig. 11.

Table 4
Cases A-1 to A-12 ($T_i = T_{max}$).

Case No.	a_0	a (mm)	T_i/A_P (MPa)	T_{real}/A_P (MPa)	$P_{b,s}$ (kN)	$P_{b,s}/P_{b,u}$	Buckling mode	After prestressing			At the onset of buckling		
								$S_l = S_r$ (kN)	N (kN)	S_l/N (%)	S (kN)	N (kN)	$N/P_{b,s}$
A-1	0	120	1373	1038	233.5	1.99	Antisymmetric	19.6	308.9	6.3	1.9	267.2	1.14
A-2	0	110	1155	883	273.0	2.33		15.3	263.1	5.8	2.2	215.3	0.79
A-3	0	100	955	738	295.4	2.52	Mixed	11.6	220.2	5.3	4.5	169.3	0.57
A-4	0	90	774	605	276.1	2.36	Symmetric	8.6	180.7	4.8	13.0	129.2	0.47
A-5	0	80	612	482	255.7	2.18		6.1	144.1	4.2	12.9	95.6	0.37
A-6	0	70	468	372	230.9	1.97		4.1	111.3	3.7	10.2	68.7	0.30
A-7	0	60	344	269	202.1	1.73		2.6	80.5	3.2	2.9	47.3	0.23
A-8	0	50	239	190	176.3	1.50		1.5	56.9	2.6	1.6	28.3	0.16
A-9	0	40	153	121	151.6	1.29		0.8	36.3	2.1	0.7	11.9	0.08
A-10	0	30	86	67	126.0	1.08		0.6	37.8	1.6	0.6	10.2	0.08
A-11	0	20	38	29	118.6	1.01		0.1	8.7	1.1	0.3	6.4	0.05
A-12	0	10	10	6	117.2	1.00		0.0	1.8	0.5	0.0	0.0	0.00

682 MPa, both the buckling capacity and the reinforcing efficiency increased, and this increase was more pronounced when $\sigma_{PS,P}$ > 300 MPa. However, when the yield strength continued to increase from 682 to 960 MPa, the buckling capacity and reinforcing efficiency did not further increase. (2) For specimens with a large slenderness (140 or 200), the influence of the yield strength on T_{opt} was very limited. For specimens with a small slenderness (105), T_{opt} increased as the steel yield strength increased. In general, for specimens that had a relatively small slenderness (λ <140) and were made of normal strength steel (f_y < 682 MPa), T_{opt} was less than that of the specimens with a greater slenderness (λ > 140) or those made of high-strength steel (f_y > 682 MPa). (3) For specimens with the same yield strength, as the slenderness increased, the buckling capacity decreased, the reinforcing efficiency increased, and T_{opt} decreased. (4) When the yield strength increased from 345 to 960 MPa, the utilization rate of the steel strength was increased because of the PS CFRP reinforcement. Specifically, the yield strength of I105-U-960 was 178% higher than that of I105-U-345, but its buckling capacity was only 3% higher than that of I105-U-345. After its reinforcement with the PS CFRP, the buckling capacity of I105-800-960 was 38% higher than that of I105-800-345. However, this phenomenon was not as pronounced when the yield strength increased from 682 to 960 MPa. Specifically, the buckling capacities of all specimens of the I105-$\sigma_{PS,P}$-682 series were as high as those of the I105-$\sigma_{PS,P}$-960 series ($\sigma_{PS,P}$ = 0,100,…800, 904). Thus, the application of PS CFRP reinforcing technology to steel columns with a high yield strength is recommended.

As shown in Fig. 17(b), the reinforcing efficiency was pronounced for most specimens ($P_{b,s}/P_{b,u}$⩾1.24), except for the specimen with a low yield strength and small slenderness (I105-0–345), for which the $P_{b,s}/P_{b,u}$ value was 1.08. This phenomenon occurred because the buckling in this case was controlled by the yield of the margin edge, and no prestressing was applied. Thus, when designing a specimen with a small slenderness (λ⩽105), a high CFRP initial prestressing force or a high yield strength (f_y⩾682 MPa) must be implemented to achieve a good reinforcing efficiency.

4.3. Influence of the CFRP elastic modulus on specimens under axial loading

I140-PS in Table 3 was taken as an example in this analysis, and its imperfection at the midspan was considered to be 0.02%L. In addition to the elastic modulus of the CFRP (E_P) of 171 GPa, E_P values of 100 GPa, 200 GPa and 250 GPa were considered. Assuming T_i = T_{max}, four specimens labeled Cases 184 to 187 were designed, as shown in Table 7. The buckling capacity $P_{b,u}$ of the corresponding unreinforced specimen was 117.2 kN.

The results are shown in Fig. 18 and Table 7. All the specimens exhibited symmetric buckling modes. As the elastic modulus of the CFRP increased, both the buckling capacity and the reinforcing efficiency both increased.

4.4. Influence of the boundary conditions on specimens under axial loading

4.4.1. L is constant

The influence of the boundary conditions on the reinforcing efficiency when the steel column length L was constant was examined in

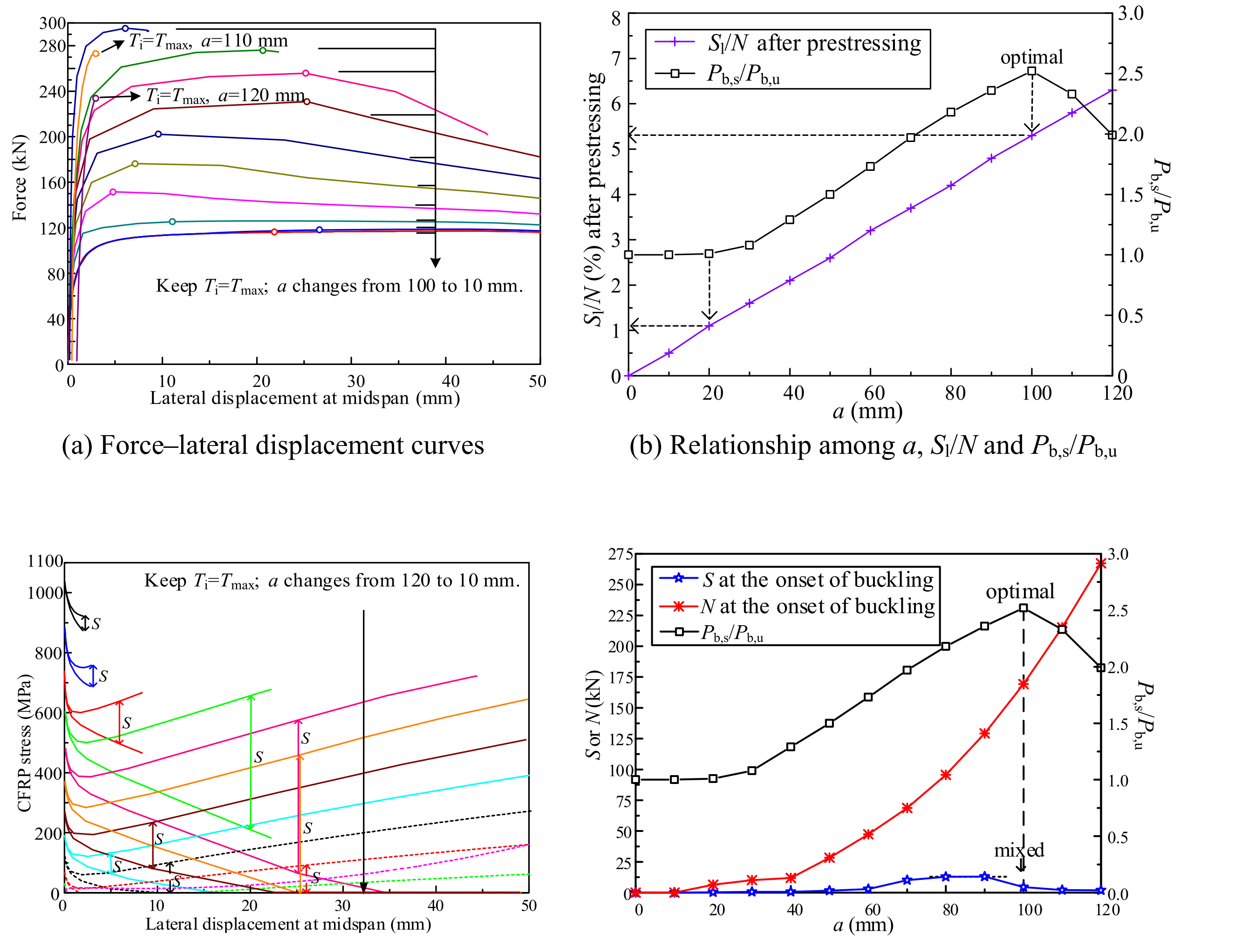

(a) Force–lateral displacement curves

(b) Relationship among a, S_l/N and $P_{b,s}/P_{b,u}$

(c) CFRP stress and lateral displacement

(d) Relationships among a, S, N and $P_{b,s}/P_{b,u}$

Fig. 13. Influence of T_i and a ($T_i = T_{max}$).

Table 5
Cases B-0 to Case B-8 ($T_i = T_{certain}$).

Case No.	a (mm)	a_0 (mm)	T_i/A_P (MPa)	T_{real}/A_P (MPa)	$P_{b,s}$ (kN)	$P_{b,s}/P_{b,u}$	Buckling mode	After prestressing			At the onset of buckling	
								$S_l = S_r$ (kN)	N (kN)	S_l/N (%)	S (kN)	N (kN)
B-0	130	120	242	192	345.0	2.94	Antisymmetric	3.9	57.5	6.82	0.7	3.3
B-1	120	109	241	188	309.5	2.64	Symmetric	3.6	56.3	6.31	3.4	13.4
B-2	110	98	239	189	303.6	2.59		3.3	56.6	5.79	2.5	10.7
B-3	100	86	239	189	297.9	2.54		3.0	56.6	5.27	1.8	9.3
B-4	90	75	239	189	272.2	2.32		2.7	56.6	4.75	1.7	13.3
B-5	80	62	240	189	245.2	2.09		2.4	56.6	4.22	2.5	15.2
B-6	70	49	242	189	218.8	1.87		2.1	56.6	3.70	1.3	21.7
B-7	60	34	236	190	200.9	1.71		1.8	56.9	3.17	1.7	24.4
B-8 (A-8)	50	0	239	190	176.3	1.50		1.5	56.9	2.65	1.6	28.3

this section. Three specimens (i.e., I140-U, I140-S and I140-PS) with two hinged end supports were used as reference specimens. When the two hinged end supports were changed to one hinged end and one fixed end support, the corresponding specimens were named I98-U-hf, I98-S-hf, and I98-PS-hf. When two fixed end supports were considered, the corresponding specimens were named I70-U-ff, I70-S-ff, and I70-PS-ff. The boundary conditions could be expressed by parameters k_1 and k_2, as shown in Fig. 2. The imperfection at the midspan was considered 0.01% L.

Table 8 and Fig. 19 show the calculation results, including the buckling capacity, force/CFRP stress–displacement curves and supporting force S at the onset of buckling. When the steel column length L was constant, under the boundary conditions of two ends hinged, one end hinged and one end fixed, and two ends fixed, the non-PS CFRP-reinforced specimen exhibited very limited improvement, whereas the PS CFRP-reinforced specimen exhibited increases of 99%, 39% and 15% in buckling capacity compared with that of the pure steel column. As the constraints of boundary conditions became stronger (k_1 or k_2 increased), the reinforcing efficiency decreased. This phenomenon occurred because the strong constraints of boundary conditions decreased the

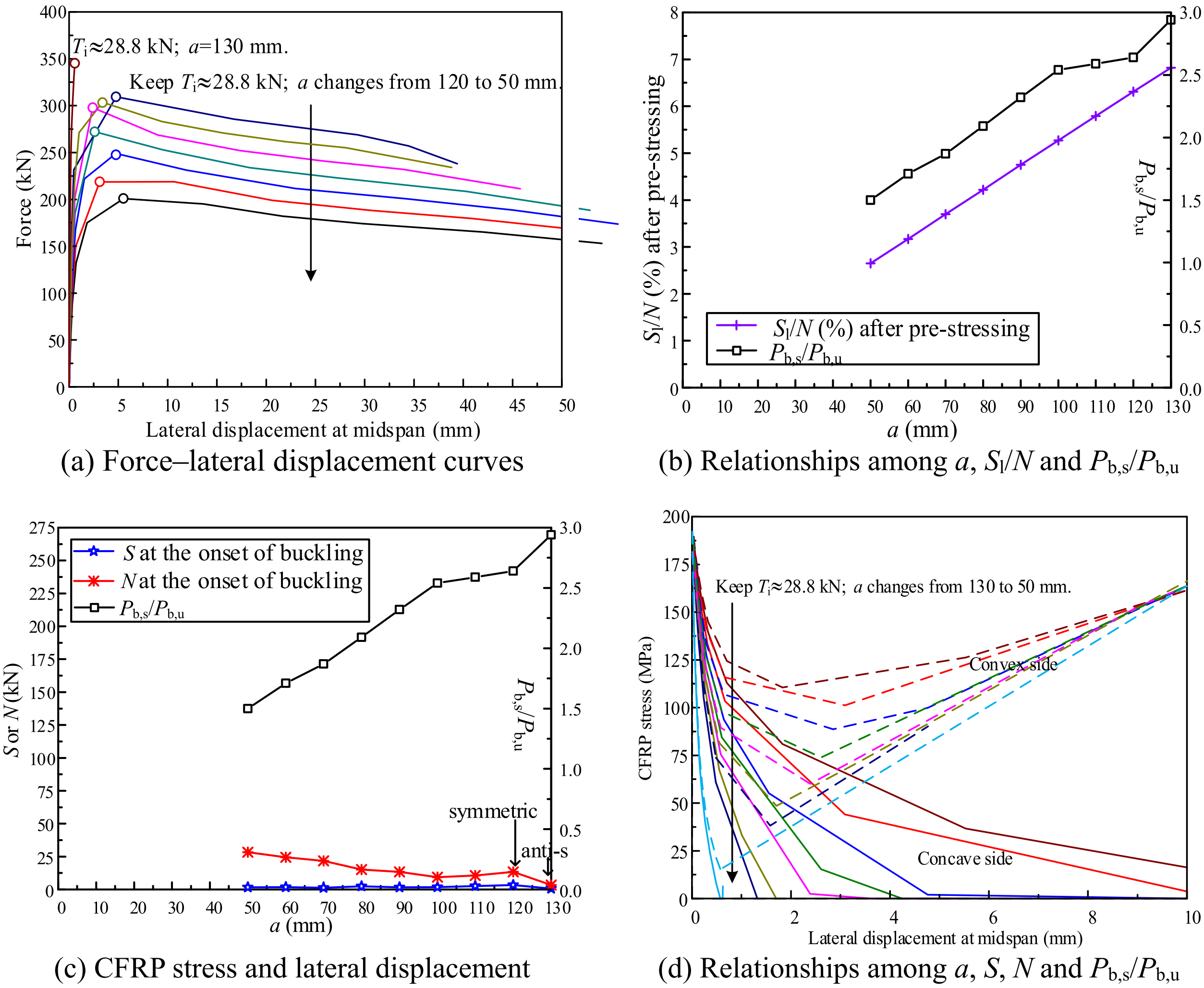

Fig. 14. Influence of T_i and a ($T = T_{certain}$).

Table 6
Cases C-0 to Case C-12 ($T = T_{min} = 0$).

Case No.	$a_0 = a$ (mm)	α (°)	$L_{P,0} + 2L_a = L_P + 2L_a$ (mm)	$P_{b,s}$ (kN)	$P_{b,s}/P_{b,u}$	Buckling mode	S at the onset of buckling (kN)	N at the onset of buckling (kN)
C-0	130	7.8	2167.8	237.9	2.03		14.1	51.2
C-1	120	7.2	2165.2	223.4	1.91		12.9	50.8
C-2	110	6.6	2162.8	208.9	1.78		10.9	46.7
C-3	100	6.0	2160.6	194.4	1.66		9.3	43.8
C-4	90	5.4	2158.6	180.5	1.54		7.6	40.0
C-5	80	4.8	2156.8	167.2	1.43		6.1	36.2
C-6	70	4.2	2155.2	154.9	1.32	Symmetric	5.1	34.2
C-7	60	3.6	2153.8	143.9	1.23		3.7	29.1
C-8	50	3.0	2152.6	134.4	1.15		2.5	23.5
C-9	40	2.4	2151.7	126.7	1.08		1.5	17.4
C-10	30	1.8	2151.0	121.1	1.03		0.7	10.6
C-11	20	1.2	2150.4	117.8	1.01		0.1	2.9
C-12	10	0.6	2150.1	117.2	1.00		0.0	0.0

slenderness of the steel column, and according to Section 3.2, the PS CFRP reinforcement was less significant for specimens with a smaller slenderness. This phenomenon can also be understood as follows. As the constraints of boundary conditions became stronger, the lateral deformation of the steel column developed more slowly; thus, the supporting force S developed more slowly and was smaller at the onset of buckling. For specimens that exhibited symmetric buckling, a smaller value of S led to a less significant reinforcing efficiency.

4.4.2. λ is constant

Four PS CFRP-reinforced specimens were designed to study the influence of the boundary conditions on the buckling capacity and reinforcing efficiency when the steel column slenderness λ was constant, as shown in Table 9. The initial imperfection at the midspan was considered to be 0.01%L.

The results show that the PS CFRP-reinforced specimens with two hinged ends exhibited the highest reinforcing efficiency. Specifically, for I98-PS-hh, the buckling capacity $P_{b,u}$ before reinforcement was 224 kN,

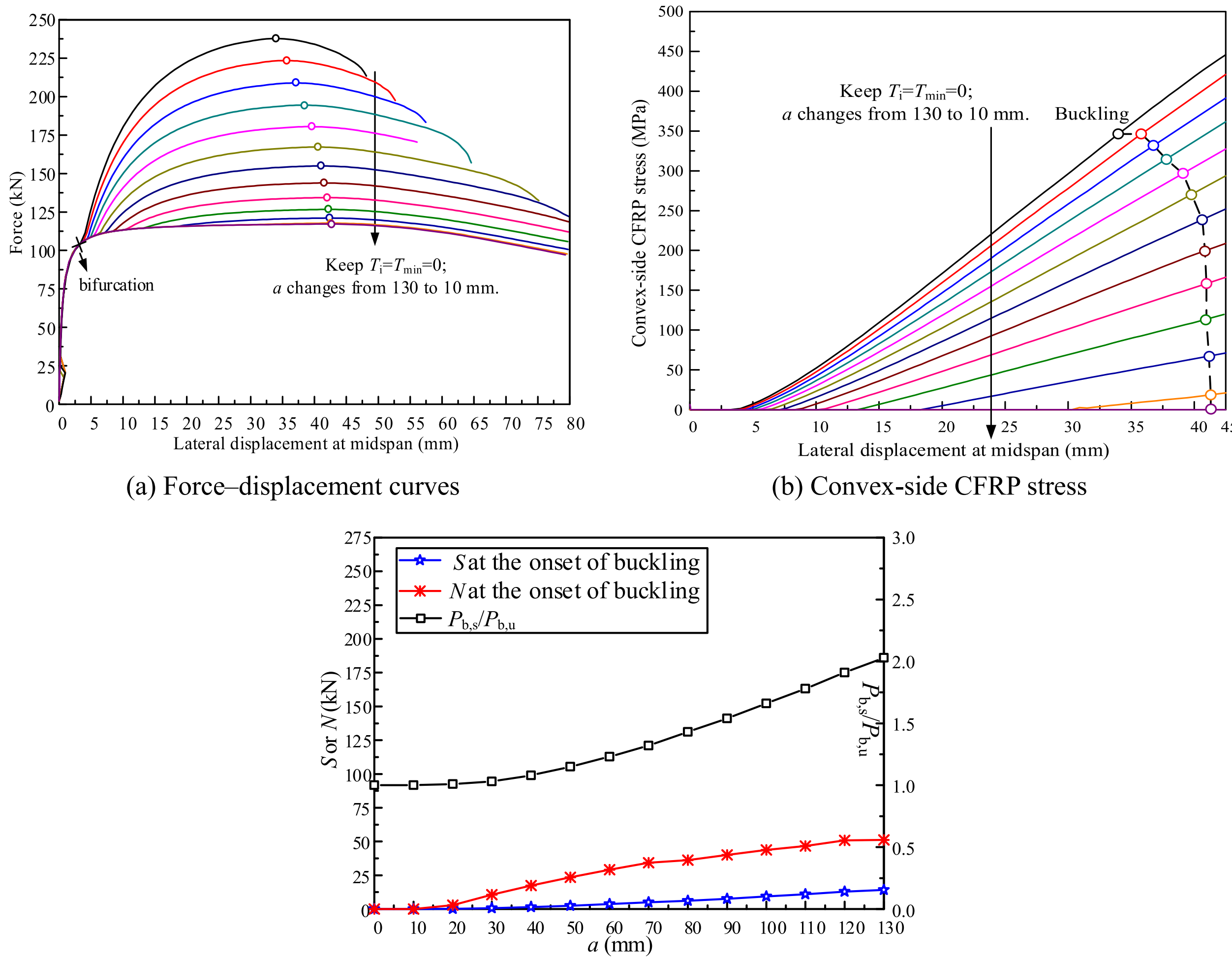

(c) Relationships among a, S, N and $P_{b,s}/P_{b,u}$ at the onset of buckling

Fig. 15. Influence of T_i and a ($T_i = T_{min}$).

same as the buckling capacity of I98-PS-hf. The buckling capacity $P_{b,s}$ after PS CFRP reinforcement was 409 kN, exceeding that of I98-PS-hf (311 kN). This phenomenon occurred because the boundary conditions of one hinged end and one fixed end were not symmetric, and thus, the maximum lateral displacement was not at the midspan; however, the prestressing chair was placed at the midspan, owing to which, the support of the PS CFRP was not fully utilized. Furthermore, for I70-PS-hh, the buckling capacity $P_{b,u}$ before reinforcement was 435 kN, same as the buckling capacity of I70-PS-ff. The buckling capacity $P_{b,s}$ after reinforcement was 543 kN, exceeding that of I70-PS-ff (500 kN). The reason for this phenomenon is shown in Fig. 20. Because the supporting length a was constant, the angle α_1 of the steel column with two hinged ends was larger than that of the steel column with two fixed ends (α_2), and tanα_1 equaled 2tanα_2. Therefore, the former case corresponded to a higher reinforcing efficiency.

4.5. Influence of the initial imperfection on specimens under axial loading

According to the real measurement of the initial imperfection after reinforcement [32], its shape is similar to a single-wave sinusoid for most specimens; thus, only the value rather than the shape of the initial imperfection is considered as a parameter in this analysis.

In the above analysis, the reduction in the initial imperfection by PS CFRP reinforcement, as described in the literature [32], was not considered; i.e., the initial imperfection at the steel column midspan after reinforcement, v_{om}, was the same as that before reinforcement, $v_{om,0}$. Section 4.5.1 continues to ignore this reduction and Section 4.5.2 considers this reduction.

4.5.1. Without considering the reduction in the initial imperfection by PS CFRP reinforcement

Four values of v_{om}, specifically, 0.02%L, 0.05%L, 0.10%L, and 0.20%L were considered. First, to study the influence of the initial imperfection on the buckling capacity and reinforcing efficiency of PS CFRP, I140-PS from Table 3 was taken as an example. All the parameters were derived from Table 3 except for the CFRP initial prestressing force T_i and initial imperfection v_{om}, which were set as variables. T_i/A_P was set to range from 0 to 500 MPa, and v_{om} was set as 0.02%L, 0.05%L, 0.10%L and 0.20%L. According to the FEM results, the corresponding unreinforced specimen of I140-PS with initial imperfections of 0.02%L, 0.05%L, 0.10%L and 0.20%L had buckling capacities $P_{b,u}$ of 117.2 kN, 115.4 kN, 112.6 kN and 107.7 kN, respectively. The buckling capacities and reinforcing efficiencies of I140-PS with these initial imperfections are shown in Fig. 21. As the initial imperfection increased, both the buckling capacity and the reinforcing efficiency decreased. This tendency was not obvious when T_i was low and became more obvious as T_i increased. Thus, a good reinforcing efficiency could be easily achieved when v_{om} was small.

Second, to investigate the influence of the initial imperfection on the maximum buckling capacity $P_{b,max}$ and optimal reinforcing efficiency $P_{b,max}/P_{b,u}$, additional specimens were considered. I140-PS (supporting length a changing from 50 to 100 mm), I105-PS and I200-PS from

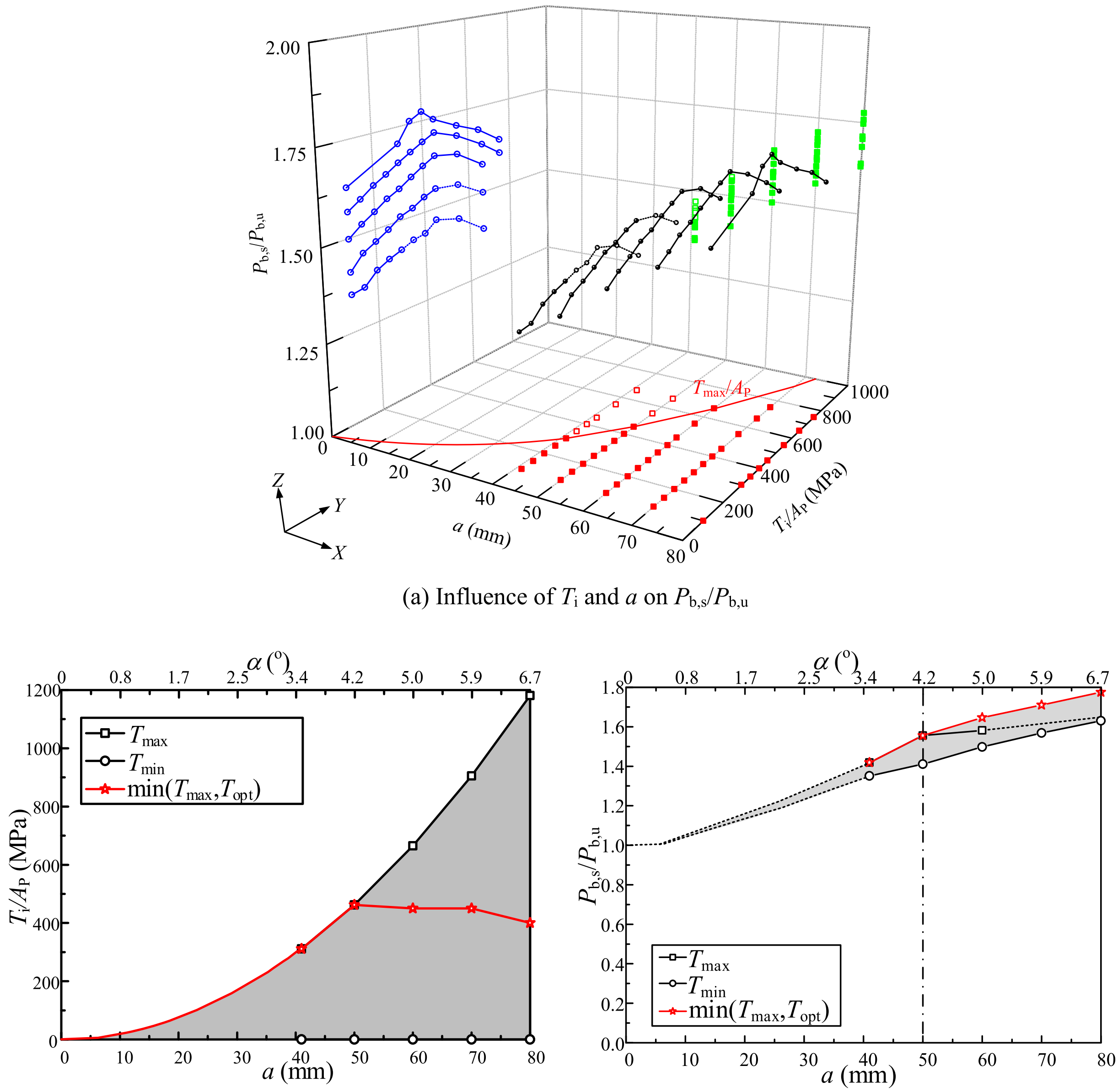

(a) Influence of T_i and a on $P_{b,s}/P_{b,u}$

(b) X-Y plane: relationship of T_i and a

(c) X-Z plane

Fig. 16. Influence of T_i and a on the reinforcing efficiency under eccentric loading.

Table 3 were examined, as shown in Table 10. The T_i value for these specimens changed from T_{min} to T_{max}, and their initial imperfection v_{om} was set as 0.02%L, 0.05%L, 0.10%L and 0.20%L.

First, the buckling capacities of the 8 specimens in Table 10 were calculated, and $P_{b,max}$ was obtained. Next, $P_{b,max}$ was divided by its value for the specimen with an initial imperfection of 0.02%L, and this ratio was defined as r, which is a reduction factor caused by the increase in the initial imperfection from 0.02%L. Thus, for every initial imperfection, the 8 specimens had 8 values of r, which could be statistically analyzed, as shown in Fig. 22. As v_{om} changed from 0.02%L to 0.05%L, 0.10%L, and 0.20%L, $P_{b,max}$ decreased by 4%, 8%, and 15%, respectively. In addition, when v_{om} was small, the rate of reduction in $P_{b,max}$ was high, and this rate decreased as v_{om} increased.

The corresponding buckling capacities ($P_{b,u}$) before reinforcing I105-PS with initial imperfections of 0.02%L, 0.05%L, 0.10%L and 0.20%L were 201.2 kN, 196.9 kN, 190.5 kN, and 179.8 kN, respectively; the corresponding values of I200-PS with initial imperfections of 0.02%L, 0.05%L, 0.10%L and 0.20%L were 58.5 kN, 57.7 kN, 57.3 kN and 55.5 kN, respectively. On the basis of these findings, the influence of v_{om} on $P_{b,max}/P_{b,u}$ is shown by the hollow point line in Fig. 22. The results indicate that as v_{om} increased, $P_{b,max}/P_{b,u}$ decreased at an approximately constant rate.

4.5.2. Considering the reduction in the initial imperfection by PS CFRP reinforcement

According to reference [32], the initial imperfection can be reduced by PS CFRP reinforcement, and the influence of this aspect was examined in this section. On the basis of this paper [32], it is assumed that $v_{om} = 50\% v_{om,0}$. The results are shown in Table 11 and Fig. 23 (solid point line). As $v_{om,0}$ and v_{om} increased, $P_{b,max}$ and $P_{b,max}/P_{b,u}$ decreased.

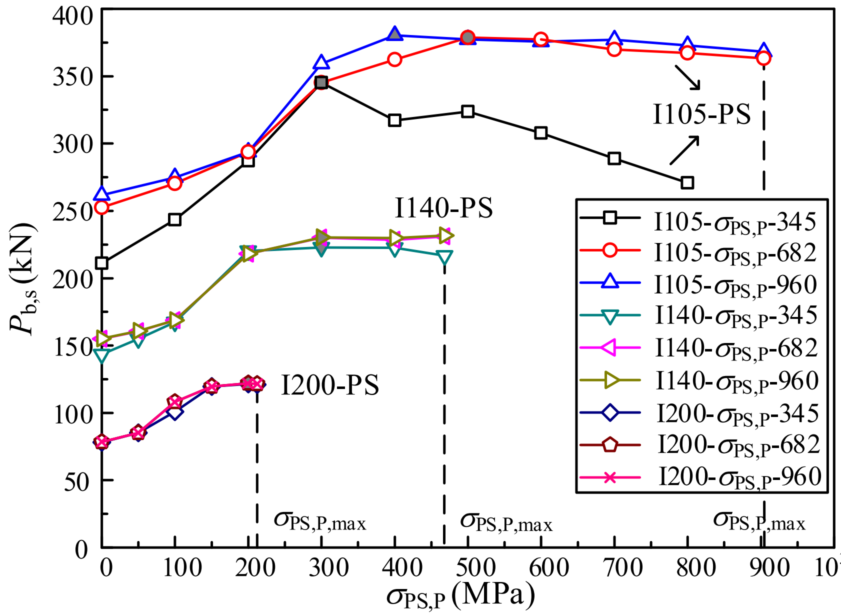

(a) Influence of λ and f_y on $P_{b,s}$

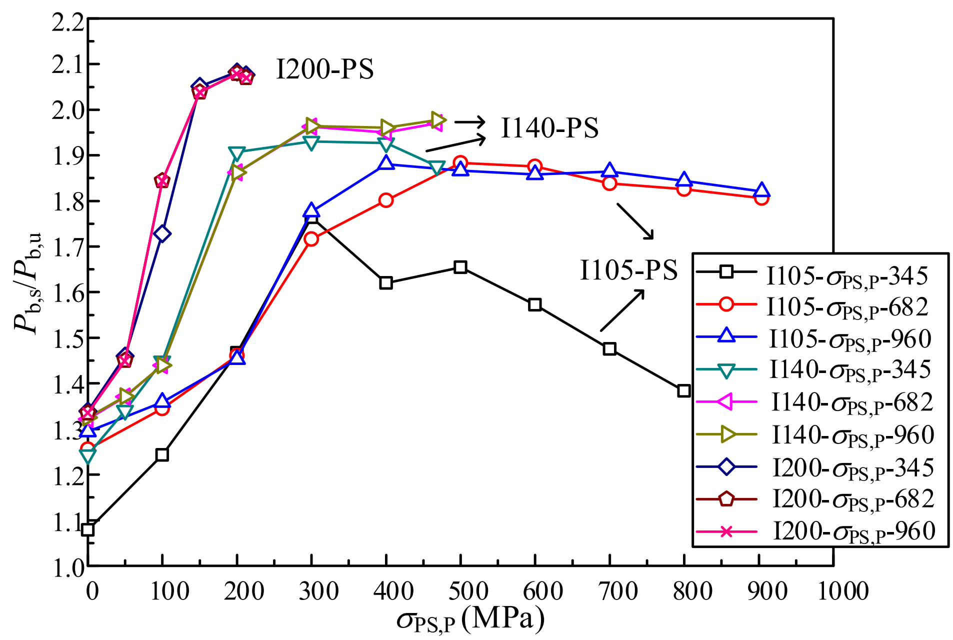

(b) Influence of λ and f_y on $P_{b,s}/P_{b,u}$

Fig. 17. Influence of slenderness and yield strength on buckling capacity and reinforcing efficiency.

Table 7
Buckling capacity and reinforcing efficiency of I140-PS with different CFRP elastic moduli.

Case No.	Specimen	E_P (GPa)	$T_i/A_P = T_{max}/A_P$ (MPa)	$P_{b,s}$ (kN)	$P_{b,s}/P_{b,u}$
184	I140-PS-E_P100	100	800	160.2	1.37
185	I140-PS-E_P171 (Case 6-a)	171	468	230.9	1.97
186	I140-PS-E_P200	200	400	248.1	2.12
187	I140-PS-E_P250	250	320	255.7	2.18

A comparison of the hollow point line, which does not consider the initial imperfection reduction by PS CFRP, and solid point line is presented in Fig. 23. It shows that the mechanism of reducing the initial imperfection by PS CFRP reinforcement can further increase the reinforcing efficiency by 6% on average and 11% at most, and this parameter is not considerably influenced by the value of $v_{om,0}$ in the range of 0.05%L to 0.2%L.

4.6. Summary of the influencing rules of the key parameters

The influencing rules of the 9 key parameters are summarized in Table 12. If an increase in a parameter led to an increase (or decrease) in the buckling capacity $P_{b,s}$ or reinforcing efficiency $P_{b,s}/P_{b,u}$, the

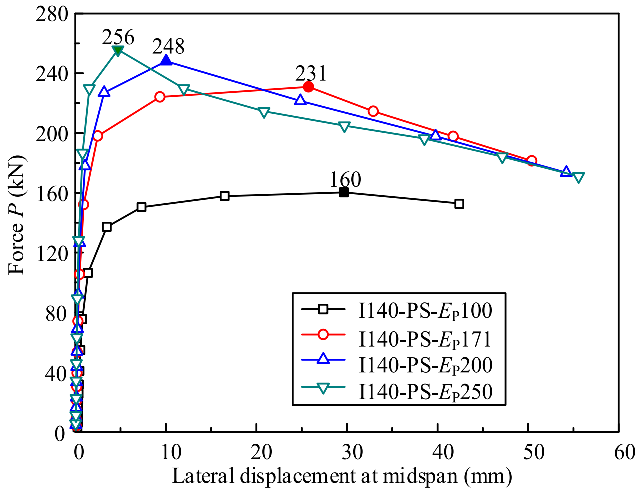

Fig. 18. Force–lateral displacement curves of I140-PS with different CFRP elastic moduli.

Table 8
Influence of boundary conditions on the buckling capacity and reinforcing efficiency (L is constant).

Case No.	Specimen	Boundary conditions	Slenderness	P_b (kN)	$P_{b,s}/P_{b,u}$	S at the onset of buckling (kN)
188	I140-U	$k_1 = k_2 = 0$	140	118	1.00	0
189	I140-S		140	121	1.03	0
190	I140-PS		140	235	1.99	4.5
191	I98-U-hf	$k_1 = 0$ $k_2 = +\infty$	98	224	1.39	0
192	I98-S-hf		98	224	1.39	0
193	I98-PS-hf		98	311	1.39	3.8
194	I70-U-ff	$k_1 = k_2 = +\infty$	70	435	1.15	0
195	I70-S-ff		70	435	1.15	0
196	I70-PS-ff		70	500	1.15	2.7

parameter was positively (or negatively) correlated to $P_{b,s}$ or $P_{b,s}/P_{b,u}$. For brevity, positive and negative correlations are labeled "positive" and "negative" in Table 12, respectively. If a parameter had a limited influence on $P_{b,s}$ or $P_{b,s}/P_{b,u}$, "limited" is presented.

5. Predicting buckling capacity with a practical ANN tool

The buckling capacity of a PS CFRP-reinforced steel column is determined by the 14 parameters (see Fig. 2). Owing to its complicated mechanism, an approach based on a practical ANN tool was adopted to predict the buckling capacity of a specimen that had an E_s of 206 GPa, included the steel and CFRP section shown in Fig. 3(a), and involved two hinged end supports. All parameters in Fig. 2 except E_s, I_s, A_s, A_P, k_1 and k_2 were regarded as 8 input variables. The buckling capacity was considered the output variable. Including the FEM cases presented in Sections 3 and 4 and additional ones from FEM, a total of 312 cases were used as samples for the ANN, among which 216 samples were randomly chosen to develop the ANN model, and the remaining 96 samples were used to evaluate the proposed model. All the data of 312 cases are listed in the supplementary material.

The back propagation (BP) algorithm [34] has demonstrated remarkable power owing to its self-learning and self-adapting characteristics. Therefore, this algorithm has been widely used in training feedforward neural networks for supervised learning to more effectively address multifactor and nonlinearity problems [35] and was adopted in this paper. The proposed ANN consists of an input layer, an output layer and a hidden layer. The input data propagate to the output layer through the hidden layer, and the error between the actual output values and target output values is propagated backward. The weights and bias at each neuron are modified to minimize the defined error function results by utilizing the gradient descent method.

In this section, 12 learning algorithms were tested to find the best algorithm for accelerating the convergence of the BP learning algorithm, as shown in Table 13. All the algorithms except Bayesian regularization randomly separated the dataset of the 216 samples into a training set, validation set and testing set, and the separation was performed according to the ratios defined by default (trainRatio: 0.7, valRatio: 0.15, and testRatio: 0.15), that is, 152 samples were used for training. The Bayesian regularization algorithm randomly separated the dataset of the 216 samples into a training set and testing set, and the separation was performed according to the ratios defined by default (trainRatio: 0.8 and testRatio: 0.2), that is, 173 samples were used for training, and the remaining 43 samples were used for testing.

To compare the algorithms, the mean square error (MSE) values of the best validation performance were utilized for all algorithms except Bayesian regularization; the MSE value of the best training performance was utilized for Bayesian regularization. The MSE can be expressed as in Eq. (5), where N is the number of samples, and t_i and y_i are the target and predicted values of the i^{th} sample, respectively. The Levenberg–Marquardt algorithm (trainlm) and Bayesian regularization (trainbr) outperformed the other algorithms because of the following reason: The Levenberg–Marquardt algorithm combines the advantages of the neural network gradient descent method and Gauss–Newton method. The function is a combination algorithm to perform smoothing and harmonizing between Newton's method and the steepest descent method, which can reduce the defects of the BP algorithm, such as low iteration speeds and tendency to easily fall into a local optimum. Furthermore, Bayesian regularization (trainbr) is a network training function that updates the weight and bias values according to the Levenberg–Marquardt optimization. The function minimizes a combination of squared errors and weights and later determines the correct combination to produce a network that performs a reasonable generalization for difficult, small or noisy datasets. According to the best epoch in Table 13, although Bayesian regularization (trainbr) requires more time, it can achieve the best performance for the data considered in this paper, with a value of 6.2e-5 at the 212th epoch. Therefore, the Bayesian regularization algorithm was adopted in the current ANN model.

The activation functions for the hidden and output layers of the proposed model were chosen as TANSIG (Eq. (6)) and PURELIN (Eq. (7)), respectively, where x and y denote the input and predicted values, respectively. The main purpose of network training was to optimize the network generalization by minimizing the errors in the output. The standard for halting the network training process was set considering the MSE. The empirical approach [36] was applied to configure the range of node numbers in the hidden layer of the proposed ANN model. The trial-and-error method was adopted to determine the appropriate number of hidden layers and number of hidden-layer nodes in the proposed neural network model, as illustrated in Fig. 24. Finally, one hidden layer with 13 hidden-layer nodes was selected. The robustness of the ANN model can be ensured because the input variables were selected based on the FEM database, the redundant input variables were eliminated, the model structure was determined according to the size and structure of the given dataset, and the best learning algorithm was selected through comparison.

$$\mathrm{MSE} = \frac{1}{N}\sum_{i=1}^{N}(t_i - y_i)^2 \tag{5}$$

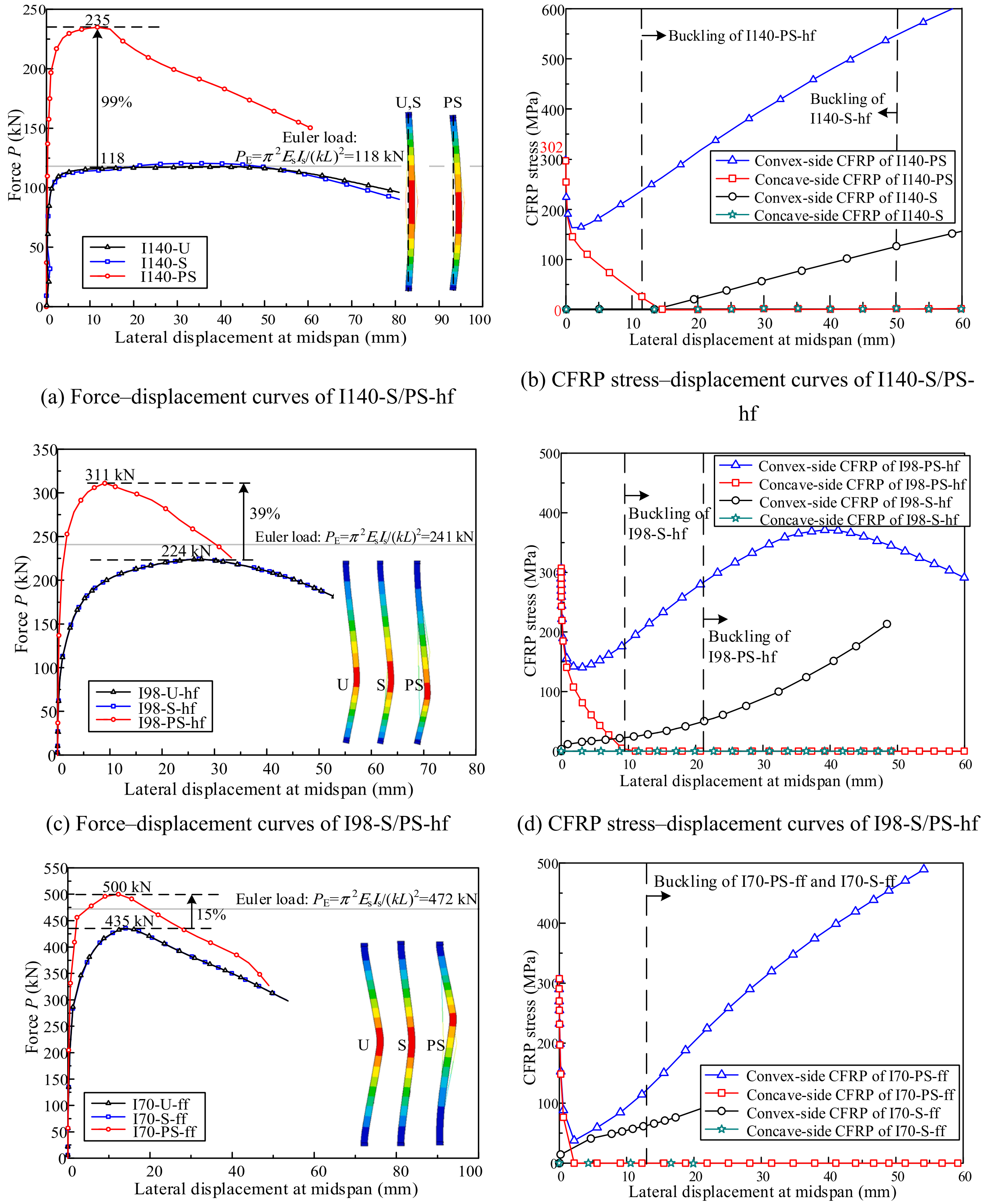

(a) Force–displacement curves of I140-S/PS-hf

(b) CFRP stress–displacement curves of I140-S/PS-hf

(c) Force–displacement curves of I98-S/PS-hf

(d) CFRP stress–displacement curves of I98-S/PS-hf

(e) Force–displacement curves of I70-S/PS-hf

(f) CFRP stress–displacement curves of I70-S/PS-hf

Fig. 19. Influence of boundary conditions on the force/CFRP stress–displacement curves (L is constant).

$$y = \mathrm{TANSIG}(x) = \frac{2}{(1+e^{-2x})} - 1 \tag{6}$$

$$y = \mathrm{PURELIN}(x) = x \tag{7}$$

$$\mathrm{MRE} = \frac{1}{N}\sum_{i=1}^{N}\frac{(y_i - t_i)}{t_i} \tag{8}$$

The simulation experiments were carried out with MATLAB [37] on

Table 9
Influence of boundary conditions on the buckling capacity and reinforcing efficiency (λ is constant).

Case No.	Specimen	Boundary conditions	λ	L (mm)	$P_{b,u}$ (kN)	$P_{b,s}$ of PS CFRP-reinforced steel column (kN)	$P_{b,s}/P_{b,u}$
197	I98-PS-hh	$k_1 = k_2 = 0$	98	1500	224	409	1.83
198	I98-PS-hf	$k_1 = 0$ $k_2 = \infty$		1050		311	1.39
199	I70-PS-hh	$k_1 = k_2 = 0$	70	1075	435	543	1.25
200	I70-PS-ff	$k_1 = k_2 = \infty$		537.5		500	1.15

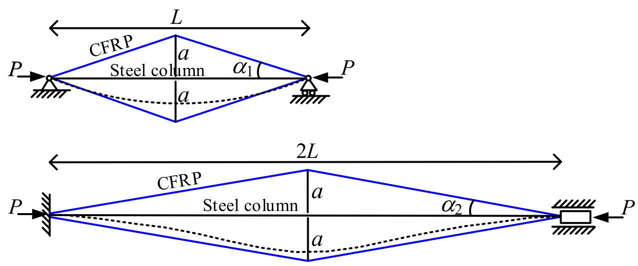

Fig. 20. Reasons for different reinforcing efficiencies of steel columns under the same λ and different boundary conditions.

a computer with an i7 4850HQ processor, a 2.3 GHz CPU, 16 Gb of 1600 MHz DDR3 memory and Mac OS. Fig. 25 shows the performance of the proposed ANN model, which illustrates the performance of the MSE indexes in the training and testing processes in each generation. Fig. 26 shows the regression coefficients of training and testing in the proposed model, where Y and T represent the normalized predicted and target values, respectively. The best-fit linear regression line between the outputs and targets is represented by a solid line. The values of the correlation coefficient R for the training, testing and all data were found to be 0.99957, 0.99375, and 0.99878, respectively, which indicated that the training produced good results.

Finally, the remaining 96 samples were used to evaluate the proposed ANN model, and the results are presented in Fig. 27. The values of the mean, standard deviation, and coefficient of variation of the ratio of P_b from the ANN to P_b from the FEM were 1.00178, 0.04799 and 0.04790, respectively, which showed the high accuracy of the ANN model. To ensure the practicality of the proposed model, a graphical user interface was implemented in MATLAB, as shown in Fig. 28, which could be used to predict the buckling capacity of the reinforced columns and obtain optimal reinforcing parameters to realize a high reinforcing efficiency.

The sensitivity level of the proposed ANN model to the uncertainty in different variables was investigated by conducting a sensitivity analysis (SA) via the mean relative error (MRE), as expressed in Eq. (8). When the input parameter value was changed randomly, the deviation between the input and output values of the proposed ANN model indicated the sensitivity of the model to the uncertainty in the input parameter. In this study, the reference value was the original MRE (2.70%). For each input parameter, a series of values between 0 and 1 was generated in intervals of 0.1 to replace the normalized input parameter values in the evaluating dataset, while keeping other input parameters unchanged, and 1056 samples were rebuilt. The normalized input data were applied to the proposed ANN model. Fig. 29 shows the results of the SA for the input parameters. The sensitivity of most input parameters to the network output was low. Specifically, the variations in f_y, v_{om}/L, T_i/A_P, and L_a had limited impact on the output value, and the MRE values were between 20% and 30%; the variation in v_{om}/L had the least impact, and the corresponding MRE value was only 15.93%. Only the changes in L and e considerably influenced the output of the proposed ANN model, and the MRE values were 76.29% and 72.88%, respectively, but the probability of abnormal values of these two parameters was low in practical engineering. Since a lower sensitivity corresponds to better robustness, the proposed model was concluded to be robust [38,39]. In addition, due to only a slight change in E_P in the entire database, an SA was not conducted for this aspect. All the SA data are listed in the supplementary material.

6. Conclusions

This paper provides an in-depth analysis of the buckling behavior of PS CFRP-reinforced steel columns, as determined through FEM and ANN techniques. The available experimental data were used to validate the proposed FEM model. Then, the validated model was used to investigate the influence of the key parameters on the buckling capacity and reinforcing efficiency of these columns. Finally, using a large number of datasets based on the validated finite element model, an approach to predict the buckling capacity of PS CFRP-reinforced steel columns was presented. The following conclusions could be derived:

(1) The proposed numerical FEM model could accurately predict the buckling characteristics of PS CFRP-reinforced steel columns, and the reinforcing efficiency of PS CFRPs was demonstrated by more than 300 FEM examples.

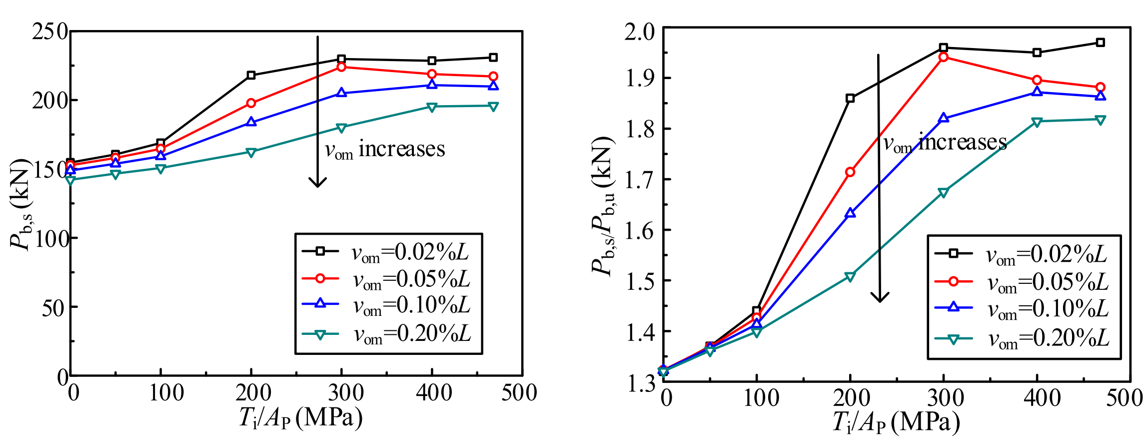

(a) Buckling capacity (b) Reinforcing efficiency

Fig. 21. Influence of initial imperfection on the buckling capacity and reinforcing efficiency ($v_{om} = v_{om,0}$).

Table 10
Influence of the initial imperfection on the maximum buckling capacity and optimal reinforcing efficiency ($v_{om} = v_{om,0}$).

Case No.	Specimen	a (mm)	$P_{b,max}$ (kN)				$P_{b,max}/P_{b,u}$			
			$v_{om}/L =$ 0.02%	$v_{om}/L =$ 0.05%	$v_{om}/L =$ 0.10%	$v_{om}/L =$ 0.20%	$v_{om}/L =$ 0.02%	$v_{om}/L=$ 0.05%	$v_{om}/L=$ 0.10%	$v_{om}/L=$ 0.20%
From 201 to 204	I140-PS	50	176.8	173.6	165.8	155.4	1.51	1.50	1.47	1.44
From 205 to 208	I140-PS	60	200.4	196.9	185.0	175.4	1.71	1.71	1.64	1.63
From 209 to 212	I140-PS	70	231.5	224.0	213.3	195.8	1.98	1.94	1.89	1.82
From 213 to 216	I140-PS	80	260.6	247.6	236.6	220.3	2.22	2.15	2.10	2.05
From 217 to 220	I140-PS	90	292.2	276.6	263.9	244.1	2.49	2.40	2.34	2.27
From 221 to 225	I140-PS	100	320.6	306.8	290.5	268.1	2.74	2.66	2.58	2.49
From 226 to 229	I105-PS	41	269.3	260.8	248.9	233.3	1.34	1.32	1.31	1.30
From 230 to 233	I200-PS	78	135.4	126.7	124.6	112.5	2.31	2.20	2.17	2.03

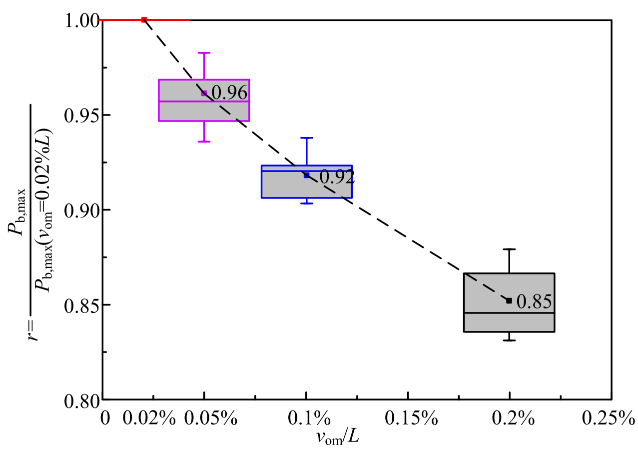

Fig. 22. Influence of initial imperfection on the maximum buckling capacity ($v_{om} = v_{om,0}$).

(2) The influence of the key parameters on the buckling capacity and reinforcing efficiency were obtained through parametric analysis. First, when the CFRP initial prestressing force ensured that the concave-side CFRP was in tension when buckling occurred, as the supporting length increased, the buckling mode changed from symmetric to mixed to antisymmetric. The buckling capacity of the specimens exhibiting mixed buckling reached or approached the maximum buckling capacity. Second, for specimens exhibiting symmetric buckling, the following influencing rules were found. As the horizontal supporting force S increased, the reinforcing efficiency increased. As the steel column slenderness increased, the buckling capacity decreased, and the reinforcing efficiency increased. As the steel yield strength increased, the buckling capacity and reinforcing efficiency increased if the slenderness was small. As the CFRP elastic modulus increased, the buckling capacity and reinforcing efficiency both increased. As the initial imperfection increased, the buckling capacity and reinforcing efficiency both decreased. In addition, considering the reduction in the initial imperfection by PS CFRP reinforcement, the reinforcing efficiency of the studied specimens further increased up to 11%.

Table 11
Influence of the initial imperfection on the optimal reinforcing efficiency ($v_{om} = 50\% v_{om,0}$).

Case No.	Specimen	a (mm)	$P_{b,max}/P_{b,u}$		
			$v_{om} = 0.5v_{om,0} = 0.02\%L$	$v_{om} = 0.5v_{om,0} = 0.05\%L$	$v_{om} = 0.5v_{om,0} = 0.10\%L$
From 234 to 236	I140-PS	50	1.53	1.54	1.54
From 237 to 239	I140-PS	60	1.74	1.75	1.72
From 240 to 242	I140-PS	70	2.01	1.99	1.98
From 243 to 245	I140-PS	80	2.26	2.20	2.20
From 246 to 248	I140-PS	90	2.53	2.46	2.45
From 249 to 251	I140-PS	100	2.78	2.72	2.70
From 252 to 254	I105-PS	41	1.37	1.37	1.38
From 255 to 257	I200-PS	78	2.35	2.21	2.25

(3) The reliable neural network tool developed in this study could accurately predict the buckling capacity of PS CFRP-reinforced steel columns. The values of the mean, standard deviation, and coefficient of variation of the ratio of P_b determined by the ANN to P_b determined by the FEM were 1.00178, 0.04799 and 0.04790, respectively. Therefore, this tool could help achieve a high reinforcing efficiency by providing prompt predictions.

Declaration of Competing Interest

The authors declare that they have no known competing financial interests or personal relationships that could have appeared to influence the work reported in this paper.

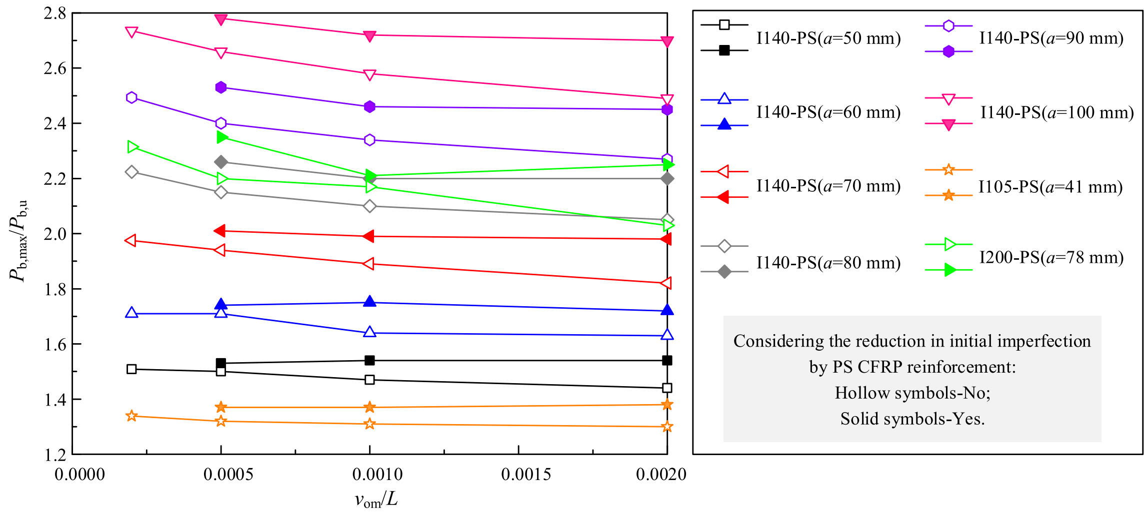

Fig. 23. Influence of initial imperfection on $P_{b,max,}/P_{b,u}$.

Table 12
Summary of the influencing rules of the 9 key parameters.

Parameters		$P_{b,s}$	$P_{b,s}/P_{b,u}$
Steel column	λ or L	Negative	Positive
	f_y	When λ is large: limited When λ is small: positive within certain limits	When λ is large: limited When λ is small: positive within certain limits
	v_{om}	Negative	Negative
CFRP	E_P	Positive	Positive
Design	a	Positive	Positive
	T_i	When $T_i < T_{opt}$: positive When $T_i > T_{opt}$: negative	When $T_i < T_{opt}$: positive When $T_i > T_{opt}$: negative
Boundary condition	e	Negative	Positive
	k_1, k_2	Positive	Negative

Table 13
Comparison of the performance of different learning algorithms.

No.	Algorithm	Acronym	Best performance	Best epoch
1	**Levenberg–Marquardt**	**trainlm**	**0.000463**	**15**
2	**Bayesian regularization**	**trainbr**	**0.000062**	**212**
3	Scaled conjugate gradient backpropagation	trainscg	0.002358	45
4	Gradient descent with momentum backpropagation	traingdm	0.475110	1
5	Gradient descent with adaptive lr backpropagation	traingda	0.006526	128
6	Gradient descent w/momentum & adaptive lr backpropagation	traingdx	0.003274	165
7	Resilient backpropagation (Rprop)	trainrp	0.003513	36
8	Scaled conjugate gradient backpropagation	traincgf	0.002388	41
9	Powell–Beale conjugate gradient backpropagation	traincgb	0.004538	12
10	BFGS quasi-Newton backpropagation	trainbfg	0.001643	68
11	Polak–Ribiere conjugate gradient backpropagation	traincgp	0.002445	35
12	One step secant backpropagation	trainoss	0.003978	20

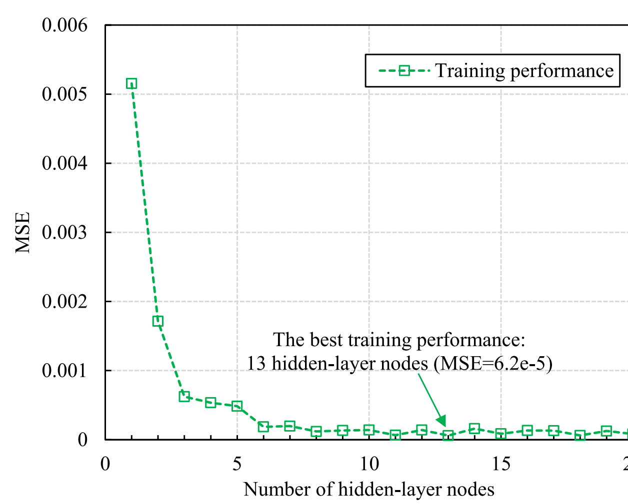

Fig. 24. MSE versus the number of hidden-layer nodes.

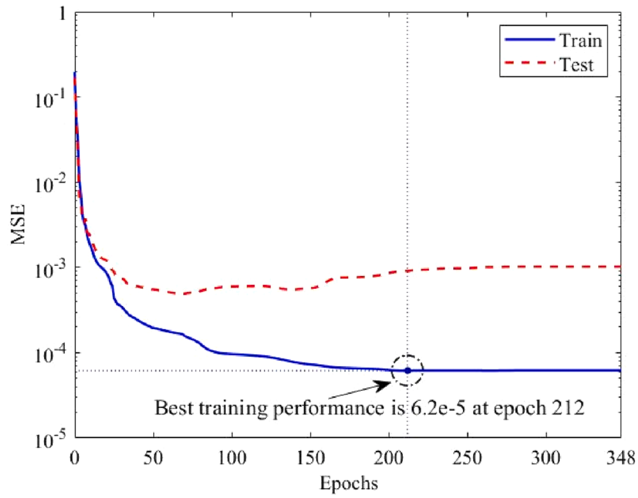

Fig. 25. Performance of the proposed model.

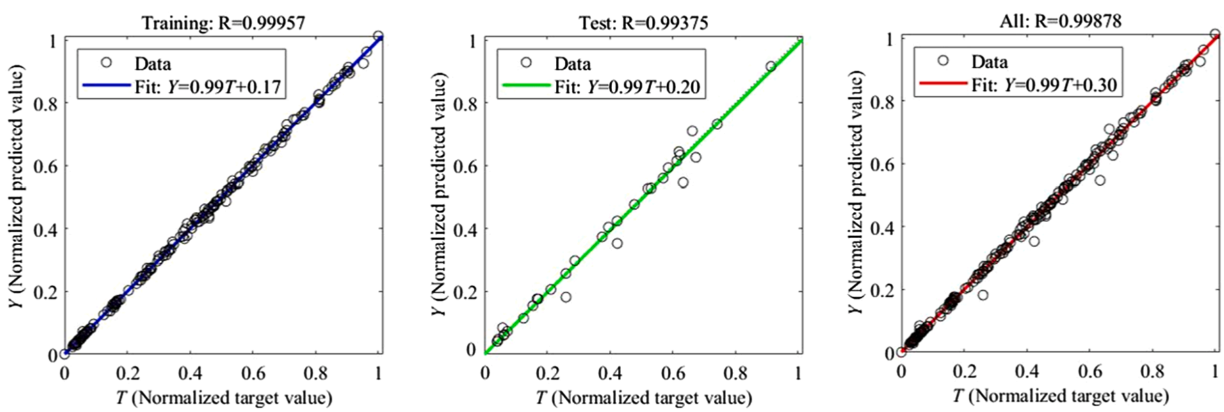

Fig. 26. Regression of the proposed model.

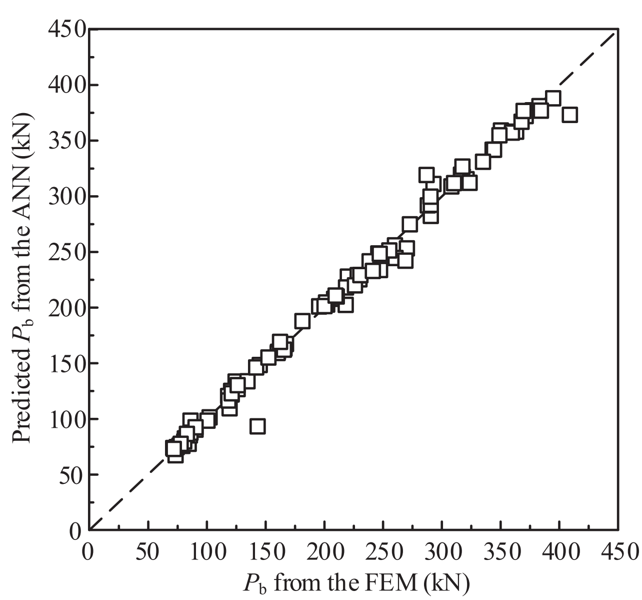

Fig. 27. Evaluation of ANN: comparison between the buckling capacity determined by the FEM and ANN.

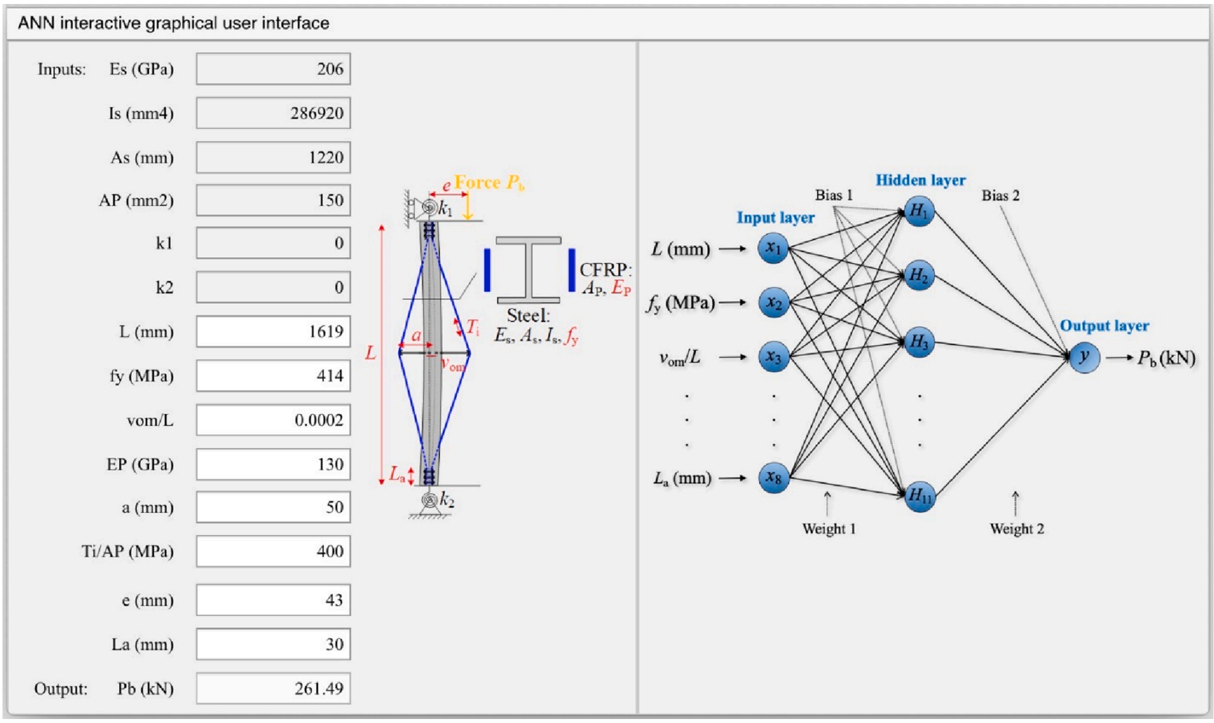

Fig. 28. GUI of the proposed ANN.

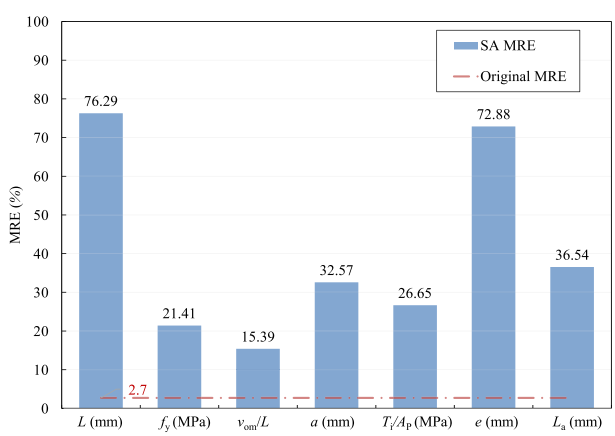

Fig. 29. Sensitivity analysis of input parameters.

Acknowledgements

This research was supported by the National Key Research and Development Program of China (No. 2017YFC0703001), the National Natural Science Foundation of China (No. 51522807), Shanghai Sailing Program (No. 21YF1419500) and start-up funding provided by Shanghai Jiao Tong University.

Declaration of competing interests

The authors declare that they do not have any commercial or associative interests that represent a conflict of interest in connection with the work submitted.

Data Availability

All the data of the ANN model and SA are provided in supplementary material.

Appendix A. Supplementary material

Supplementary data to this article can be found online at https://doi.org/10.1016/j.engstruct.2021.112853.

References

[1] Chen S. Stability of Steel Structures: Theory and Design. Beijing: Science Press; 2008.
[2] Jiang S. China Quarantine Hotel Collapse Left 29 People Dead, CNN, Beijing; 2020.
[3] Marzouk H, Mohan S. Strengthening of wide-flange columns under load. Can J Civ Eng 1990;17(5):835–43. https://doi.org/10.1139/l90-094.
[4] Tall L. The reinforcement of steel columns. Eng J 1989;26:33–7.
[5] Maquoi R, Skaloud M. Stability of plates and plated structures: general report. J Constr Steel Res 2000;55(1-3):45–68. https://doi.org/10.1016/S0143-974X(99)00077-2.
[6] Gao XY, Balendra T, Koh CG. Buckling strength of slender circular tubular steel braces strengthened by CFRP. Eng Struct 2013;46:547–56. https://doi.org/10.1016/j.engstruct.2012.08.010.
[7] Feng P, Zhang Y, Bai Y, Ye L. Combination of bamboo filling and FRP wrapping to strengthen steel members in compression. J Compos Constr 2013;17(3):347–56. https://doi.org/10.1061/(ASCE)CC.1943-5614.0000353.
[8] Feng P, Zhang Y, Bai Y, Ye L. Strengthening of steel members in compression by mortar-filled FRP tubes. Thin-Walled Struct 2013;64:1–12. https://doi.org/10.1016/j.tws.2012.11.001.
[9] Hu LL, Wang YY, Feng P, Qiang HL. Debonding development in cracked steel plates strengthened by CFRP laminates under fatigue loading: Experimental and boundary element. Thin-Walled Struct 2021;166(108038). https://doi.org/10.1016/j.tws.2021.108038.
[10] Feng P, Hu L. Steel columns strengthened/reinforced by prestressed CFRP strips: concepts and behaviors under axial compressive loads. Compos Struct 2019;217:150–64. https://doi.org/10.1016/j.compstruct.2019.03.038.
[11] Hu L, Feng P. Prestressed CFRP-reinforced steel columns under axial and eccentric compression. Compos Struct 2021;268:113940. https://doi.org/10.1016/j.compstruct.2021.113940.
[12] Ban H, Shi G, Shi Y, Wang Y. Overall buckling behavior of 460MPa high strength steel columns: experimental investigation and design method. J Constr Steel Res 2012;74:140–50. https://doi.org/10.1016/j.jcsr.2012.02.013.
[13] Shi G, Ban H, Bijlaard FSK. Tests and numerical study of ultra-high strength steel columns with end restraints. J Constr Steel Res 2012;70:236–47. https://doi.org/10.1016/j.jcsr.2011.10.027.
[14] Shaat A, Fam A. Finite element analysis of slender HSS columns strengthened with high modulus composites. Steel Compos Struct 2007;7:19–34. https://doi.org/10.12989/scs.2007.7.1.019.

[15] Devi U, Amanat KM. Non-linear finite element investigation on the behavior of CFRP strengthened steel square HSS columns under compression. Int J Steel Struct 2015;15(3):671–80. https://doi.org/10.1007/s13296-015-9013-7.
[16] Feng P, Hu L, Qian P, Ye L. Buckling behavior of CFRP-aluminum alloy hybrid tubes in axial compression. Eng Struct 2017;132:624–36. https://doi.org/10.1016/j.engstruct.2016.11.051.
[17] Teng JG, Hu YM. Behaviour of FRP-jacketed circular steel tubes and cylindrical shells under axial compression. Constr Build Mater 2007;21(4):827–38. https://doi.org/10.1016/j.conbuildmat.2006.06.016.
[18] Chu K-H, Berge SS. Analysis and design of struts with tension ties. J Struct Div 1963;89(1):127–64. https://doi.org/10.1061/JSDEAG.0000871.
[19] de Araujo RR, de Andrade SAL, Vellasco PCGdS, da Silva JGS, de Lima LRO. Experimental and numerical assessment of stayed steel columns. J Constr Steel Res 2008;64(9):1020–9. https://doi.org/10.1016/j.jcsr.2008.01.011.
[20] Saito D, Wadee MA. Numerical studies of interactive buckling in prestressed steel stayed columns. Eng Struct 2009;31(2):432–43. https://doi.org/10.1016/j.engstruct.2008.09.008.
[21] Wu K, Wadee MA, Gardner L. Prestressed stayed beam-columns: sensitivity to prestressing levels, pre-cambering and imperfections. Eng Struct 2021;226:111344. https://doi.org/10.1016/j.engstruct.2020.111344.
[22] Sampaio G, Vallim Filho A, Silva L, Silva L. Prediction of motor failure time using an artificial neural network. Sensors 2019;19:4342. https://doi.org/10.3390/s19194342.
[23] Si B, Wang J, Yao X, Shi X, Jin X, Zhou X. Multi-objective optimization design of a complex building based on an artificial neural network and performance evaluation of algorithms. Adv Eng Inform 2019;40:93–109. https://doi.org/10.1016/j.aei.2019.03.006.
[24] Chang CM, Lin TK, Chang CW. Applications of neural network models for structural health monitoring based on derived modal properties. Measurement 2018;129:457–70. https://doi.org/10.1016/j.measurement.2018.07.051.
[25] Shu J, Zhang Z, Gonzalez I, Karoumi R. The application of a damage detection method using Artificial Neural Network and train-induced vibrations on a simplified railway bridge model. Eng Struct 2013;52:408–21. https://doi.org/10.1016/j.engstruct.2013.02.031.
[26] ANSYS, Release 11.0., Documentation for ANSYS, ANSYS Inc., Canonsburg, PA; 2005.
[27] ANSYS, User's Manual. Version 10.0, Swanson Analysis Systems Inc., Houston; 2006.
[28] Ban H. Research on the Overall Buckling Behavior and Design Method of High Strength Steel Columns Under Axial Compression. Doctor Thesis. Beijing: Tsinghua University; 2012.
[29] Padmarajaiah SK, Ramaswamy Ananth. A finite element assessment of flexural strength of prestressed concrete beams with fiber reinforcement. Cem Concr Compos 2002;24(2):229–41. https://doi.org/10.1016/S0958-9465(01)00040-3.
[30] Li H, Zong P, Yang T. Research on mechanism of deformation reduced by CO_2 gas shielded arc welding. Hot Work Technol 2011;21.
[31] Zhang WF. Symmetric and antisymmetric lateral–torsional buckling of prestressed steel I-beams. Thin-Walled Struct 2018;122:463–79. https://doi.org/10.1016/j.tws.2017.10.015.
[32] Feng P, Zou YC, Hu LL, Liu TQ. Use of 3D laser scanning on evaluating reduction of initial geometric imperfection of steel column with pre-stressed CFRP. Eng Struct 2019;198:109527. https://doi.org/10.1016/j.engstruct.2019.109527.
[33] Chan Siu-Lai, Shu Gan-ping, Lü Zhi-tao. Stability analysis and parametric study of pre-stressed stayed columns. Eng Struct 2002;24(1):115–24. https://doi.org/10.1016/S0141-0296(01)00026-8.
[34] Hornik Kurt, Stinchcombe Maxwell, White Halbert. Multilayer feedforward networks are universal approximators. Neural Netw 1989;2(5):359–66. https://doi.org/10.1016/0893-6080(89)90020-8.
[35] Dahou Zohra, Mehdi Sbartaï Z, Castel Arnaud, Ghomari Fouad. Artificial neural network model for steel–concrete bond prediction. Eng Struct 2009;31(8):1724–33. https://doi.org/10.1016/j.engstruct.2009.02.010.
[36] Cai R, Cui Y, Xue PJ. Research on the methods of determining the number of hidden nodes in three layer BP neural network. Comput Inf Technol 2017;25:29–33.
[37] Matlab, Neural Networks Toolbox Release R2019a, MathWorks, Natick, MA; 2019.
[38] Dao Dong Van, Adeli Hojjat, Ly Hai-Bang, Le Lu Minh, Le Vuong Minh, Le Tien-Thinh, et al. A sensitivity and robustness analysis of GPR and ANN for high-performance concrete compressive strength prediction using a Monte Carlo simulation. Sustainability 2020;12(3):830. https://doi.org/10.3390/su12030830.
[39] Kuo YL, Jaksa MB, Lyamin AV, Kaggwa WS. ANN-based model for predicting the bearing capacity of strip footing on multi-layered cohesive soil. Comput Geotech 2009;36(3):503–16.